Response of magnesium microcrystals to *c*-axis compression and contraction loadings at low and high strain rates

Nicolò Maria della Ventura [a],[*], Amit Sharma [a], Cyril Cayron [b], Szilvia Kalácska [a],[d],
Thomas E.J. Edwards [a], Cinzia Peruzzi [a], Manish Jain [a], Julia T. Pürstl [c], Roland E. Logé [b],
Johann Michler [a], Xavier Maeder [a]

[a] *Empa, Swiss Federal Laboratories for Materials Science and Technology, Laboratory for Mechanics of Materials and Nanostructures, Feuerwerkerstrasse 39, Thun 3602, Switzerland*
[b] *Laboratory of ThermoMechanical Metallurgy (LMTM), PX Group Chair, Ecole Polytechnique Fédérale de Lausanne (EPFL), Rue de la Maladière 71b, Neuchâtel 2000 , Switzerland*
[c] *Department of Materials Science and Metallurgy, University of Cambridge, 27 Charles Babbage Road, Cambridge CB3 0FS, United Kingdom*
[d] *Mines Saint-Etienne, Univ Lyon, CNRS, UMR 5307 LGF, Centre SMS, 158 cours Fauriel, Saint-Étienne 42023, France*

A R T I C L E   I N F O

A B S T R A C T

In this work, 99.999% pure magnesium (Mg) single microcrystals have been deformed in [0001] compression (*c*-axis compression) and [10$\overline{1}$0] tension (*c*-axis contraction) conditions at room temperature and under loading rates ranging from 5×10^{-4} up to ~590 s^{-1}. The strain rate sensitivity and apparent activation volume of prismatic and pyramidal slip systems were evaluated. In *c*-axis contraction, at strain rates of 45 s^{-1}, the formation of a new grain whose crystallographic characteristics do not correspond to those of well-known twin systems could be observed. An explanation was found but it requires the breakdown of the invariant plane strain condition, and a unit cell reconstruction via pyramidal II to basal plane transformation. This unconventional twin is at 2.1° far from a classical simple shear twin on {10$\overline{1}$5} planes. In *c*-axis compression, at the highest applied strain rate, no twin could be detected in the 5 µm sized pillars of 2:1 (height to width) aspect ratio. Plasticity is thus purely mediated by slip. However, the appearance of newly oriented grains was observed by lowering the sample size or by reducing the aspect ratio. Their crystallographic features suggest a mechanism of unit cell reconstruction through the transformation from pyramidal I to basal plane. The results presented in this study impose to consider twinning as a reorientation mechanism not necessarily limited to a simple shear.

1. Introduction

Deformation twinning in hexagonal-close-packed (hcp) crystals is strongly dependent on the loading direction with respect to the crystallographic *c*-axis [1,2]. In magnesium (Mg) and its alloys, two types of *c*-axis twins are commonly reported, {10$\overline{1}$2}{10$\overline{1}$1} tension (TTW) and {10$\overline{1}$1}{10$\overline{1}$2} compression (CTW). The critical resolved shear stress (τ_{CRSS}) of TTW is lower than that for CTW [3]. The occurrence of TTW during *c*-axis tensile loading is the primary mode for accommodating the plastic deformation in almost all the experimental conditions (i.e. temperatures and strain rates [4]), whilst CTW during *c*-axis compression is known to be a minor deformation mechanism at room temperature [5–7].

CTWs have been generally observed during compression of extruded or hot-rolled polycrystalline specimens with different textures and grain sizes [3,8–10]. Due to the variation in grain orientation, the presence of grain boundaries, pre-existing twin boundaries and other complexities, externally applied and locally perceived stress states may differ, resulting in a very difficult assessment of the stress tensor at CTW nucleation sites and limiting their understanding. In the past, to overcome this problem, *c*-axis macro and microscale compression tests were performed on single crystals of pure Mg [5–7]. Indeed, although the τ_{CRSS} for slip on the close-packed basal plane is significantly lower than for the prismatic and pyramidal π1 and π2 planes, basal slip can be suppressed during *c*-axis compression due to a null Schmid factor, which favours the activity of other deformation modes, including CTW. Surprisingly, despite the uniaxial compressive stress field in such tests,

* Corresponding author.
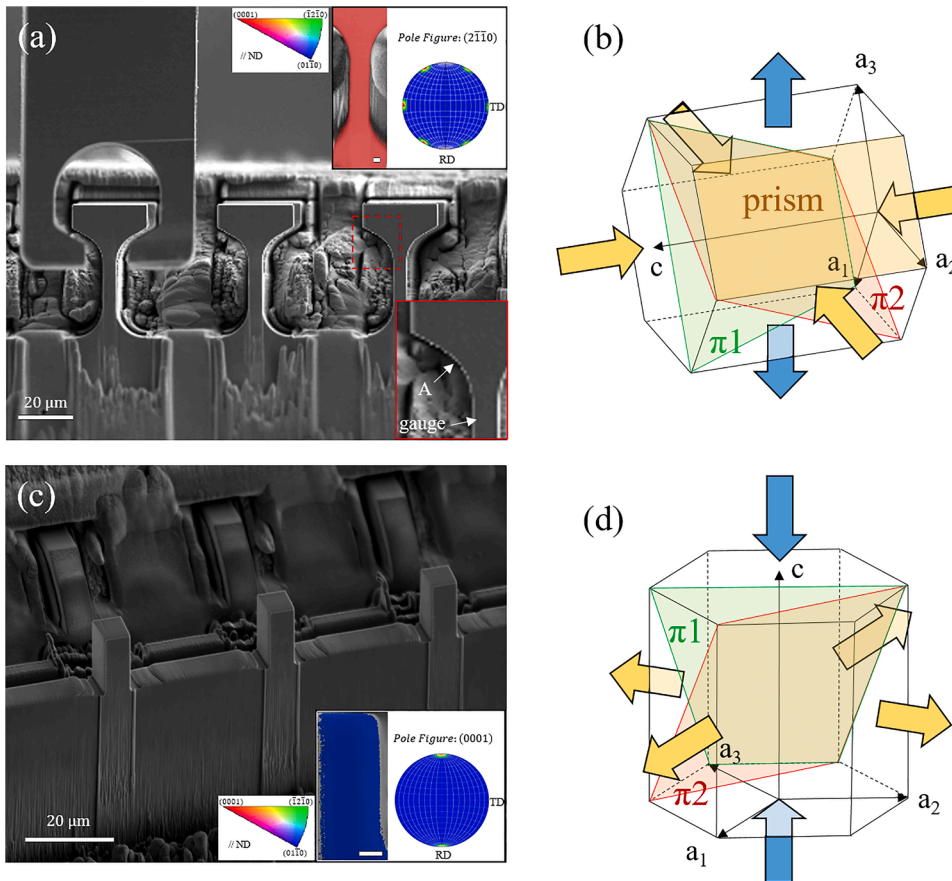 *E-mail address:* nicolo.dellaventura@empa.ch (N.M. della Ventura).

Fig. 1. SEM images of the micro-specimens fabricated by focused ion beam (FIB) and the corresponding crystallographic orientations. (a, c) Single crystal microtensile and micropillar specimens prepared at the sample edge allowing EBSD before and after deformation on the front surface. The EBSD maps and pole figures in the inserts show the respective crystal orientations. In the insert (bottom-right), "A" indicates a (triaxial) stress concentration site due to the geometry of the specimen. (b,d) Stress and strain fields of the crystal during $[10\bar{1}0]$ extension (b) and [0001] compression (d). The blue arrows indicate the externally applied stress; the yellow arrows refer to the strains induced by the action of the applied load. The slip planes along which the deformation is expected to take place are highlighted in the crystals. All undefined scale bars in the inserts correspond to 2 μm. The inverse pole figure (IPF) colour code refers to the out-of-plane crystal direction (ND, normal direction). (For interpretation of the references to colour in this figure legend, the reader is referred to the web version of this article.)

CTWs occur occasionally in areas of high stress concentration in the form of thin, needle-like lamellae, while pyramidal slip activity largely governs plasticity [6,11,12]. This has an important effect on the mechanical response of Mg. The large build-up of internal strains accommodated by limited and harder deformation modes leads to lower ductility at high strain levels and thus induces material failure, making *c*-axis compression the most detrimental loading condition in Mg. Nevertheless, [0001] compression of a single-crystal sample efficiently allows for investigation of strain rate sensitivities (*SRSs*) of non-basal slip systems and, in principle, of CTWs. To this end, as twinning is reported to be less strain rate sensitive compared to slip [13–17], and higher stress states can be reached at smaller scales, the easier activation of CTW at higher deformation rates could be suspected and could help to shed a light into the so-called "lack of CTWs".

In Mg high-stress conditions can also favour the nucleation of particular "new grains". Indeed, apart from slip and deformation twinning, another way of accommodating plasticity during *c*-axis compression of Mg was introduced very recently in the form of *deformation graining* [18]. In particular, Liu et al. [18] observed that the displacements of atoms occurring due to either the high-stress loading conditions, due to the exhaustion of dislocation mediated plasticity at high strain levels or both, induce a "hybrid diffusive-displacive" mode of deformation that results in the nucleation of newly oriented grains, not corresponding to usual deformation twins. The formation of these new grains enhances the plasticity by means of the activation of other deformation modes (slip and twinning) within them, improving the machinability of Mg and reducing crack nucleation. This mechanism cannot be directly related to deformation twinning because the existence of an invariant twin plane could not be established [19]. In view of some evidence of unusual parent-new grain misorientations and incoherent twin interfaces reported and discussed for the last decade [20], Cayron [21] suggested that deformation twins should be considered as

martensitic transformations without diffusion. The shuffles are just movements of atoms in the lattice that do not obey the same linear law as the nodes of the lattices; they are thus not related to any diffusion mechanism. The phenomenon of *deformation graining* can be thus understood without diffusion as a martensitic mechanism, by using the recently introduced *weak twinning* concept [22]. In particular, *weak twinning* refers to a mechanism in which the interface is not anymore necessarily fully invariant as for usual deformation twinning, but it can be slightly distorted to be transformed into a new non-equivalent plane.

In order to further investigate the afore-mentioned research areas, micropillar compression in [0001] and microtensile tests in $[10\bar{1}0]$ orientations were performed under loading rates from 5×10^{-4} up to $\sim 590\ \mathrm{s}^{-1}$. The shape and position of testing specimens close to the edge of the sample, allowed precise characterizations of the crystallographic orientation by Electron Backscatter Diffraction (EBSD) both before and after testing. The experiments required the redesign of the quasi-static and high strain rate (HSR) testing rigs, making them suitable for both compression and tensile loading at the microscale, and limiting divergences in the compliance of the test machines. The choice of loading directions allows for further study of the direction-dependent micromechanical response of Mg by observing the material behaviour during *c*-axis direct and indirect straining (*c*-axis compression and contraction, respectively). In particular, *c*-axis compression refers to when the externally applied stress field has a component along the [0001] direction, whilst *c*-axis contraction when the [0001] axis is reduced by the effect of a strain. This implies that *c*-axis compression and *c*-axis contraction have different associated strain fields, and hence different values of interaction work, *W* [23]. Russell et al. [8] suggested that the onset of CTW may be facilitated under *c*-axis contraction compared to *c*-axis compression due to a lower τ_{CRSS} attributed to differences in the stresses experienced by the unit cell. This behaviour was ascribed by the

Table 1

m_{SF} and τ_{CRSS} of the slip and twin systems considered for [10$\overline{1}$0] extension and [0001] compression of Mg specimens.

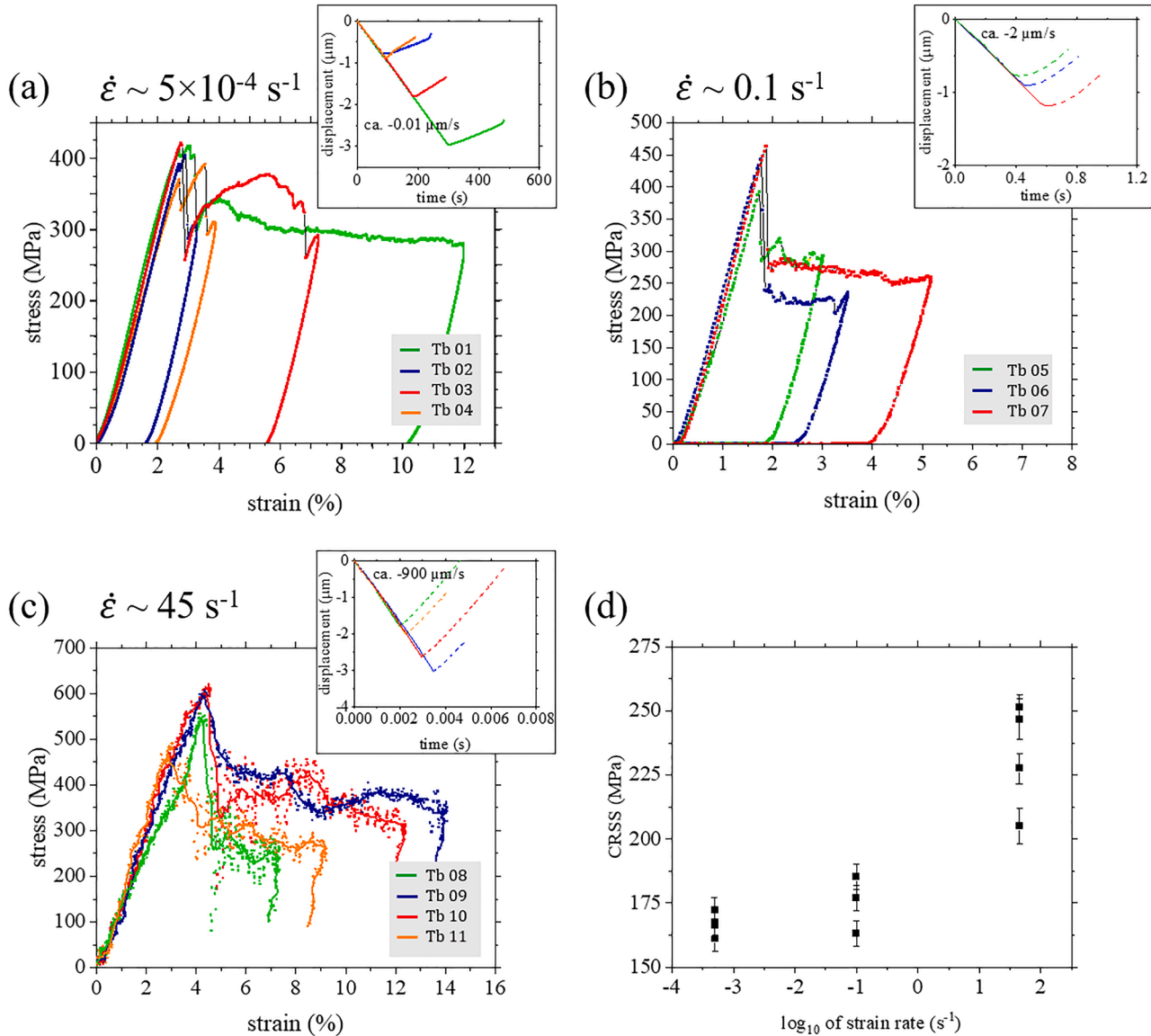| Mode	crystal direction	plane	experimental τ_{CRSS} (MPa)	<10$\overline{1}$0> tension		<0001> compression	
				m_{SF}	σ_y (MPa)	m_{SF}	σ_y (MPa)
Basal	<1$\overline{2}$10>	(0001)	0.52–0.81 [28,29]	0	-	0	-
Prismatic <a>	<1$\overline{2}$10>	(10$\overline{1}$0)	39–50 [30,31]	0.44	88–113	0	-
Pyramidal I <c+a>	<2$\overline{11}$3>	(10$\overline{1}$1)	40–44 [32,33]	0.41	97–107	0.41	97-107
Pyramidal II <c+a>	<1$\overline{2}$13>	(11$\overline{2}$2)	80 [34]	0.35	225	0.45	177
CTW	<10$\overline{1}$2>	(10$\overline{1}$1)	115 [3]	0.43	267	0.43	267

Fig. 2. Stress-strain curves related to [10$\overline{1}$0] tensile tests at different strain rates (5×10^{-4} to 45 s^{-1}) (a–c). The inserts illustrate the displacement vs time curves from which the strain rate has been calculated considering a characteristic height of 20 μm. Note that the displacement values are corrected for rig compliance. For further information regarding the displacement calibration procedure, refer to [25]. The variation of the τ_{CRSS} with strain rate is shown in (d). The value of τ_{CRSS} has been measured in correspondence of the stress that preceded the load drop detected in (a-c). Note that the error bars consider also uncertainties (±100 nm) in the SEM measurements of the dimensions of the specimens.

authors to the greater hydrostatic pressure in the case of contraction compared to the case of uniaxial *c*-axis compression, favouring the complex shuffles required for this twinning mode. As CTWs manifest themselves as thin and needle-like lamellae, 3D EBSD reconstructions have been performed to ensure the eventual "lack of CTW" through the whole thickness of some deformed specimens. A thorough investigation

of the possible nucleation of new *unconventional twins* is also presented.

2. Materials and methods

A 99.999% pure, fully single-crystalline Mg sample (PSC, Easton, USA) was mechanically polished to 1 μm and then electro-polished at 12
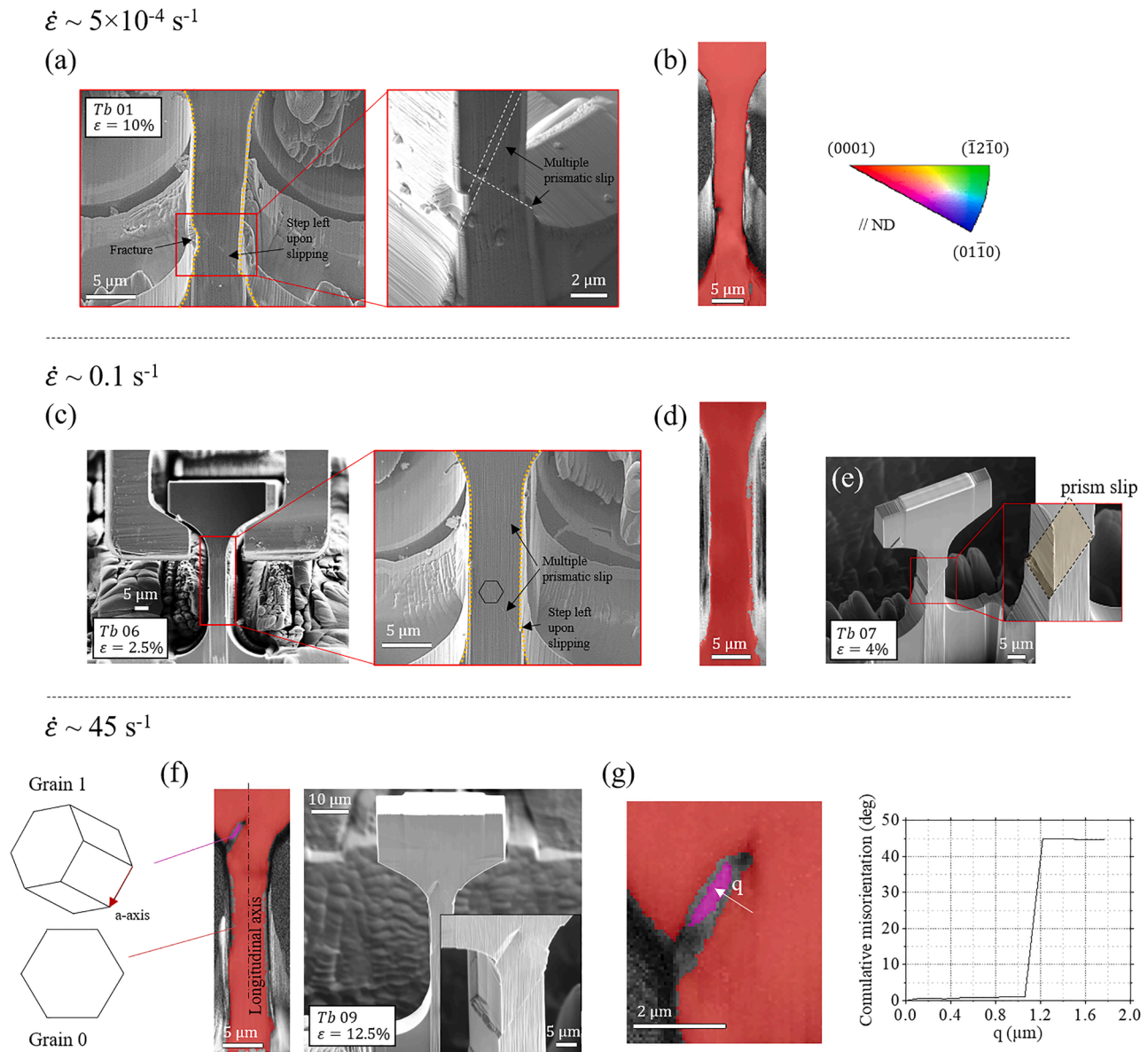
Fig. 3. SEM images and EBSD maps illustrating post-mortem deformation features in tensile specimens strained at different deformation rates. (a,b) $\dot{\varepsilon} = 5 \times 10{-}4\,\mathrm{s}^{-1}$, (c–e) $\dot{\varepsilon} = 0.1\,\mathrm{s}^{-1}$, (f,g) $\dot{\varepsilon} = 45\,\mathrm{s}^{-1}$. In all the cases, plasticity has been accommodated by prismatic slip, as clearly evincible from the slip traces detected via SEM imaging (a,c,f). For $\dot{\varepsilon} \leq 0.1\,\mathrm{s}^{-1}$, the EBSD maps (b,d) do not show any twin activity. At the highest applied strain rate, the formation of a new grain $\sim$44° ($\pm$1°) misoriented with respect to the parent crystal around the a-axis has been observed in the location of high stress concentration (indicated with letter "A" in Fig. 1) (f,g). The cumulative misorientation is plotted in (g). The IPF colour code refers to the out-of-plane crystal direction (ND).

V with a refrigerated (10 °C) electrolyte, comprised of 85% ethanol, 5% HNO$_3$ and 10% HCl. The sample was then used for microtensile bar (T-bar or Tb) and micropillar fabrication using a Ga$^+$ focused ion beam (FIB) microscope (Tescan, Lyra3) with gauge cross-section dimensions of $5 \times 5\,\mu\mathrm{m}^2$ for both specimen types, and height of 20 μm and 10 μm, respectively (see Fig. 1). Two additional sets of pillars have been fabricated with gauge cross-section dimensions of (i) $1.2 \times 1.2\,\mu\mathrm{m}^2$ with 2:1 height to width aspect ratio, and (ii) $5 \times 5\,\mu\mathrm{m}^2$ with 3:2 aspect ratio (tolerance on dimensions: $\pm$100 nm). To avoid curtaining artifacts on the lateral surfaces of the specimens, a 200 nm thick ion-beam deposited platinum layer was applied on top of them. The cross-section area was used to calculate the engineering stresses. Stresses and strains (σ, ε) are nominal. The specimens were fabricated at the top edge of the bulk sample, allowing for EBSD acquisitions before and after the deformation. The micromechanical tests were conducted using dedicated *in situ* Alemnis nanoindenter modules for quasi-static and HSR conditions [24]

mounted inside a scanning electron microscope (SEM, Tescan Lyra3). The tensile tests were then performed along the [10$\bar{1}$0] axis at different strain rates using a silicon gripper [25], whereas loading along the [0001] axis in compression employed a nanoindenter fitted with a 20 μm diameter doped diamond flat punch. In HSR compression, the testing rig employs a piezo-electric load sensor where the flat punch was mounted rather than the standard strain gauge-based load cell used at low strain rates in conventional testing conditions ($<$1 s^{-1}). In tension, the piezo-electric load sensor was mounted on the sample side.

After micromechanical testing, several micropillars were lifted out and thinned down in order to provide an overview of the textural development upon deformation. Transmission Kikuchi Diffraction (TKD) maps were recorded with an electron beam of 30 kV and 10 nA using an EDAX DigiView camera with 2×2 binning (442×442 px^2). After the TKD map acquisitions, further thinning was performed for atomic resolution imaging using a ThermoFischer Themis 200 G3 aberration
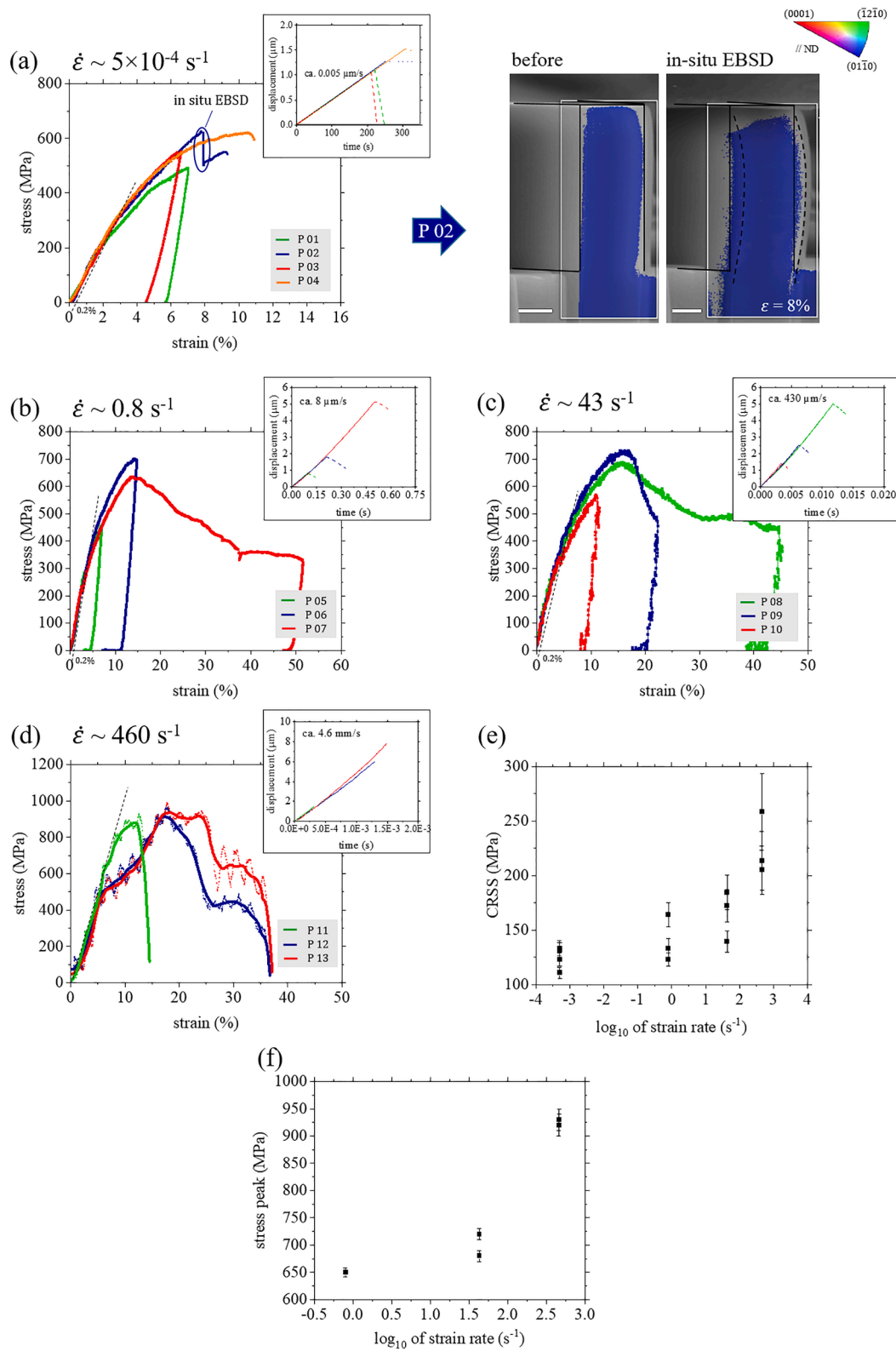
Fig. 4. Stress-strain curves for [0001] compression tests at different strain rates: from 5×10^{-4} to 460 s^{-1} (a-d). The inserts illustrate the displacement vs time curves from which the strain rate has been confirmed considering a characteristic height of 10 μm. The variation of the τ_{CRSS} with strain rate is shown in (e). The τ_{CRSS} has been measured at a plastic strain of 0.2% (a–d). Note that the error bars consider also uncertainties (±100 nm) in the SEM measures of the dimensions of the specimens. In (d), the material response is overwhelmed by the oscillation amplitude, not allowing a precise extraction of the material properties. An adjacent average smoothing procedure every 35 data points has been therefore adopted (note that the experimental sampling rate used for this condition was 1 MHz). (f) Maximum nominal stress reached in the specimens at different strain rates. All undefined scale bars correspond to 2 μm. The IPF colour code refers to the out-of-plane crystal direction (ND).

(probe) corrected Transmission Electron Microscope (TEM) operating at 200 kV. For some pillars, scanning precession electron diffraction (SPED) with a step size of 7 nm was used to generate high spatial resolution orientation/phase maps with a DigiSTAR system from Nano-MEGAS company (Brussels, Belgium) installed in the same aberration-corrected TEM.

Three-dimensional EBSD reconstructions of two deformed tensile specimens were performed to detect and reconstruct the complete shape and spatial distribution of the grains that constitute the specimen. This was done using post-mortem EBSD acquisitions together with FIB tomography in a static setup [26]. In this case, EBSD maps were acquired with a Symmetry detector and the Aztec 4.1 software (Oxford Instrument, UK), with 20 kV using 7 nA beam conditions and 150 nm step size. EBSD maps were captured after every FIB slice of 200 nm from the front surface throughout the thickness of the specimen. FIB slicing was performed at 30 kV and 1 nA. Photoshop CC 2017 was used to manually align the slices by changing the visibility of one slice over the other. Amira v5.2 software was used to create the 3D reconstructions from the 2D maps.

3. Results

Fig. 1a,c shows the $(2\bar{1}\bar{1}0)$ and (0001) pole figures for the T-bar and pillar specimens. The chosen reference system for the hcp unit cell ($\mathbf{a_1}$, $\mathbf{a_2}$, $\mathbf{c}$) can be seen in Fig. 1b,d. The Schmid factor (m_{SF}), τ_{CRSS} and $\sigma_y = \tau_{CRSS}/m_{SF}$ (yield stress) values to predict the possible and preferred modes of deformation are reported in Table 1. In both cases basal activity is inhibited through $m_{SF\_basal} = 0$. The value of τ_{CRSS} for the $\{10\bar{1}2\}$ twin mode reported for bulk Mg in the literature is low ($\sim$12 MPa) [27], however, the unidirectionality of twinning in hcp hinders its formation in c-axis compression. Thus, although the τ_{CRSS} for <a> prismatic, <c+a> pyramidal 1st and 2nd order slip planes are much higher (Table 1), they remain the only possible modes of accommodating the plastic deformation, together with CTW.

3.1. [10$\bar{1}$0] tension (c-axis contraction)

In tension, the deformation behaviour is characterized by a series of discrete load drops in the stress-strain curve and a simultaneous hardening and/or stress plateau (Fig. 2a–c). In all tests, the first load drop occurred with the onset of yield after elastic loading and has been therefore used to determine the τ_{CRSS} of the corresponding activated deformation mode. The variation of the τ_{CRSS} with strain rate, from which the *SRS* is derived at yield ($SRS = \frac{\partial \ln \tau}{\partial \ln \dot{\varepsilon}}$), is reported in Fig. 2d. The calculated values of *SRS* are $\sim$0.01 and $\sim$0.046 for $\dot{\varepsilon} \leq 0.1\ s^{-1}$ and $\dot{\varepsilon} > 0.1\ s^{-1}$, respectively, which correspond to values of apparent activation volume (V^*) (using Eq. (1)) of (2.36 $\pm$ 0.2) nm^3 and (0.43 $\pm$ 0.07) nm^3.

$$V^* = k_B T \frac{\partial \ln \dot{\varepsilon}}{\partial \tau_{CRSS}}\bigg|_T \tag{1}$$

with k_B the Boltzmann constant and T the temperature at which the test was performed (293 K).

The SEM images reported in Fig. 3 show an overview of the processes that assisted plastic deformation of the microtensile specimens at the different applied strain rates. For a specific loading condition, different strain values have been applied intentionally in order to avoid the specimen failure and allow for post-test observations of the different deformation stages. Slip traces at the front and lateral surfaces of the specimens can be attributed to the activation of prismatic planes (Fig. 3e, Tb05). It was thus revealed that prismatic slip represents the predominant mode accommodating the plastic deformation during [10$\bar{1}$0] microtensile loading. Expressing therefore V^* in terms of b^3, with b the Burgers vector of <a> prismatic dislocation ($b = 0.3209$ nm), the

apparent activation volume was found to be $\sim$72b^3 for $\dot{\varepsilon} \leq 0.1\ s^{-1}$ and $\sim$13b^3 above. It needs to be pointed out that the experimental determination of V^* is of primary importance as it is related to the area swept by the dislocation and it is indicative of the dislocation mobility mechanism. In other words, the value of V^* represents a signature of the rate-controlling deformation mechanism. Rate-determining processes such as the intersection of forest dislocations are associated to large activation volume (about a few thousand b^3), whilst dislocation climb produces lower activation volumes of approximately 1b^3. Mechanisms like dislocation cross-slip, Peierls-Nabarro stress or Peierls barrier overcoming, point defect drag or interaction, are however associated to activation volume values in the range of 10–100 b^3 [35]. From this, the values obtained here suggest overcoming of Peierls barrier as a dominant rate-controlling process in the deformation of pure Mg at room temperature under c-axis contraction conditions. Notably, the help of the applied stress to overcome the energy barrier for dislocation motion becomes significant at higher strain rate, as evidenced by the reduction of V^* with strain rate.

Furthermore, at the highest applied strain rate in micro-tension (45 s^{-1}) and for the most strained specimen (Tb09), a new thin and needle-like lamellar grain was formed (Grain 1). EBSD analyses in Fig. 3f,g suggest that the matrix (Grain 0) and the new grain are related by a $\sim$44° ($\pm$1°) misorientation around the *a*-axis, in short: (44°, *a*-axis). This does not correspond to the 56.2° expected in the occurrence of CTW. Giving the limited size of Grain 1, it is important to ascertain whether other new grains, not detectable at the front surface of the specimens, have developed within specimens deformed at lower strain rates. Thus, with the intent of performing a more complete and accurate analysis, a 3D reconstruction has been made for Tb01 as well as for Tb09, which represent the most strained specimens at the lowest and highest applied strain rates (Supp Fig. S-1). From these reconstructions, no other grain was observed apart from Grain 1 in Tb09. Moreover, the latter disappears after the first 200 nm below the front surface (after the first FIB slice in the process of the 3D reconstruction – see Section 2). An *in situ* video of a tensile test carried out at the highest imposed strain rate can be found in Supplementary Video 1.

3.2. [0001] loading (c-axis compression)

In compression, the trend of the stress-strain curve is not characterized by any discrete load drop but rather by continuous plastic flow (Fig. 4). The yield stress σ_y has been therefore measured at 0.2% of strain. As for the tensile case, the variation of the τ_{CRSS} with strain rate, from which the *SRS* is derived at yield, is reported in Fig. 4e. The calculated values of *SRS,* necessarily associated with pyramidal slip due to the restricting Schmid factor, are $\sim$0.035 and $\sim$0.131 for low/intermediate ($\dot{\varepsilon} \leq 10\ s^{-1}$) and high values of strain rate ($\dot{\varepsilon} > 10\ s^{-1}$), respectively. This corresponds to activation volumes V^* of (0.72 $\pm$ 0.08) nm^3 and (0.15 $\pm$ 0.05) nm^3, which, expressed in terms of b^3 (with $b \approx$ 0.612 nm, being the Burgers vector of a <c+a> dislocation) would become $\sim$3b^3 and $\sim$1b^3, respectively. Contrarily to the activation volume values obtained for prismatic slip in c-axis contraction conditions (see Section 3.1), it appears that the climb of pyramidal <c+a> dislocations represents the dominant rate-controlling process in the deformation of pure Mg under c-axis compression conditions, in line with what reported in previous simulation results [36–38]. Additionally, despite the comparable or higher τ_{CRSS} of pyramidal I or II and prismatic slip systems (Table 1), a reduction in the absolute yield values is detected from *c*-axis contraction to *c*-axis compression for all the investigated strain rates. This is likely due to the complex tri-axial strain field in the first few-tens of nanometres below the tip-pillar contact surface in compression, which is likely to favour the activation of dislocations at smaller strain levels.

At the lowest strain rate (5 $\times$ 10^{-4} s^{-1}), the setup has been adapted to perform *in situ* HR-EBSD measurements at 8% strain (see Fig. 4a, blue curve) by maintaining the flat punch displacement at a constant value
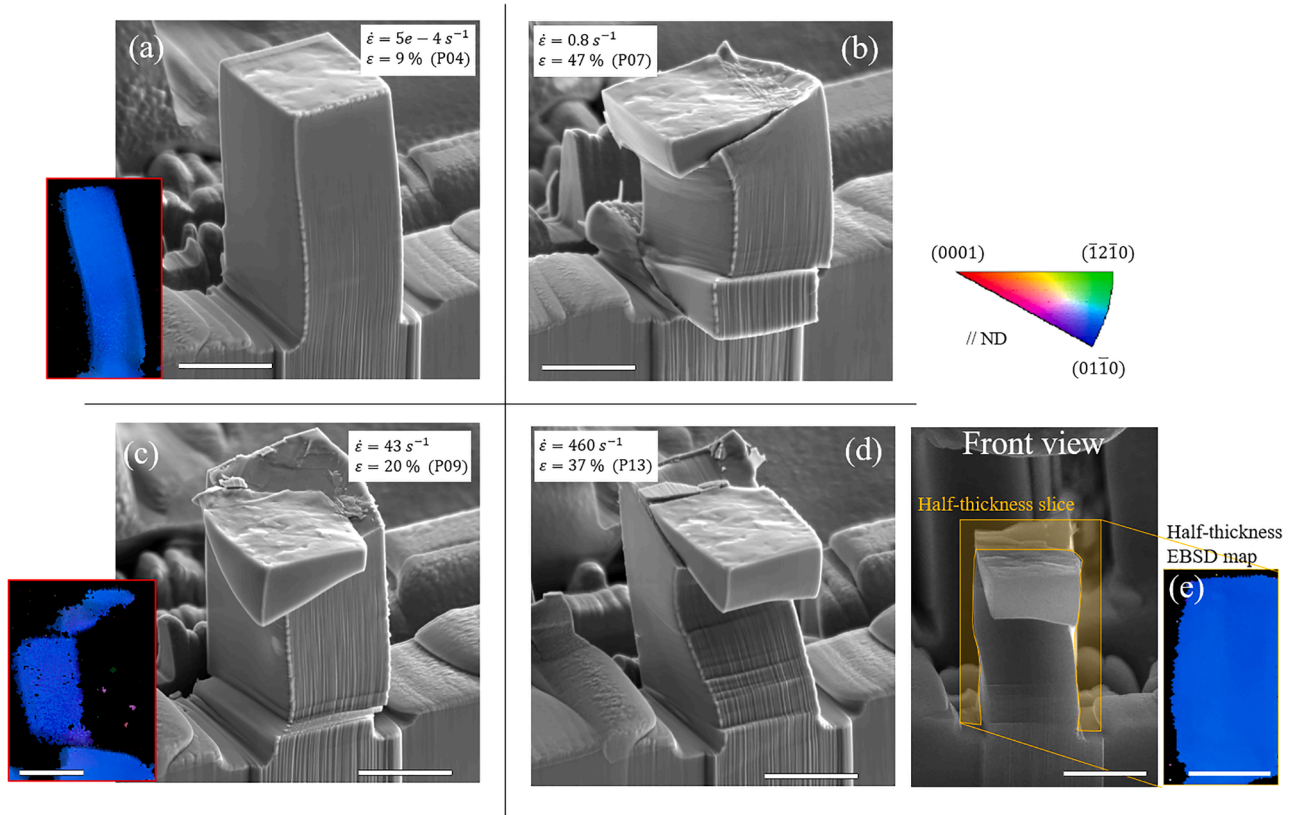
Fig. 5. SEM images and EBSD maps for pillars compressed at different strain rates. The pillar number, strain rate and level of strain achieved are indicated in each image (a-d). A bulging mechanism is observed in all specimens. A front view SEM image is shown for the pillar compressed at 460 s^{-1} (d). (e) EBSD map taken at half of the thickness of pillar P13 in (d). Plasticity is mainly accommodated by pyramidal II slip ({$11\bar{2}2$}<$11\bar{2}3$>) and basal slip ((0001)<$2\bar{1}\bar{1}0$>). No twinning mechanism was detected. All undefined scale bars correspond to 5μm. The IPF colour code refers to the out-of-plane crystal direction (ND).

while the sample was under load [39,40]. The intermediate map was captured to investigate whether the "lack of CTWs" can be caused by detwinning during unloading. However, no CTW has been detected in loaded conditions. The reduction in stress shown in Fig. 4a at $\varepsilon = 8\%$ is due to the stress relaxation occurring throughout the holding time (17 min) during which the intermediate EBSD map was taken. This relaxation is due to creep of the piezoelectric actuator and the load cell and possibly minor stress relaxation in the material. It is noted that *in situ* EBSD acquisition was not possible for the other applied strain rates as the total testing time was less than 1s (inserts in Fig. 4b–d). In Fig. 4 it can also be seen that, regardless of the imposed strain rate, a stress peak is reached at around 20% strain after which a lower load is required for further straining (softening). The magnitude of the stress peak however changes with strain rate, as reported in Fig. 4f, reaching ~900 MPa at 460 s^{-1}. Thus, Fig. 4f illustrates the maximum load that a 5μm-sized pillar (with a 2:1 height-width aspect ratio) can support during [0001] compression before ceding at different strain rates. In some cases, the misalignment between the *c*-axis and loading direction, induced by the instability of the specimen, allows basal slip activity (see Fig. 5). Despite the appearance of cleavage planes, indicative of the typical fragile nature of Mg at large strains (Fig. 5), a remarkable resistance to applied load occurs at the microscale even at HSRs for strain levels below ~20%. After testing, post-mortem EBSD maps were acquired on the front surface of each pillar without revealing the presence of CTWs or "anomalous" new grains (not relatable to well-known twinning modes). However, to investigate their possible presence inside the pillar specimens, subsequent EBSD maps have been acquired through the thickness of the pillars by FIB tomography. Again, no new twin/grain formation could be revealed for specimens with gauge cross-section dimensions of 5×5 μm^2 and aspect ratio 2:1, as also reported elsewhere [5–7].

Nevertheless, the nucleation of new grains was observed in pillars with smaller dimensions and aspect ratios. In particular, to reach higher stress levels for a given strain value, with the intent of triggering CTW or new grain formation, different pillar dimensions have been chosen and tested at HSR. Fig. 6 shows the stress-strain curves, pre- and post-deformation SEM images and SPED maps of 1.2×1.2 μm^2 (aspect ratio 2:1) and 5×5 μm^2 (aspect ratio 3:2) pillars. The smaller pillars (1.2×1.2 μm^2) have been deformed up to ~50% strain with the σ_y increasing to ~1 GPa (Fig. 6a, [41–43]), which is twice as high as what was measured for the 5×5 μm^2 pillars (Fig. 4). Using SPED it can be observed that new small grains have formed (Fig. 6c). With respect to their crystallographic nature, the parent-new grain misorientations correspond to ~62° around the *a*-axis, for both the new pillar dimensions. This does not correspond to any well-known twin mode. Similar to the increase in stress level achieved by decreasing the characteristic dimension (width) of the pillar, a reduction in the aspect ratio of the specimen from 2:1 to 3:2 (while keeping same reference dimensions: 5×5 μm^2) also affects the plasticity mechanism and the nominal stress level reached (Fig. 6b). Indeed, new grains have been observed (Fig. 6d). The *in situ* videos of compression tests carried out at the highest applied strain rates can be found in Supplementary Video 2, 3 and 4.

4. Discussion

In [$10\bar{1}0$] tension (*c*-axis contraction), the activation of prismatic slip systems (Fig. 3e, Tb05) results in (i) a stress plateau (Fig. 2a–c) representing the constant friction stress required for continuous gliding (assuming constant interfacial area) and (ii) limited further plasticity compared to that observed in *c*-axis compression, for all the applied
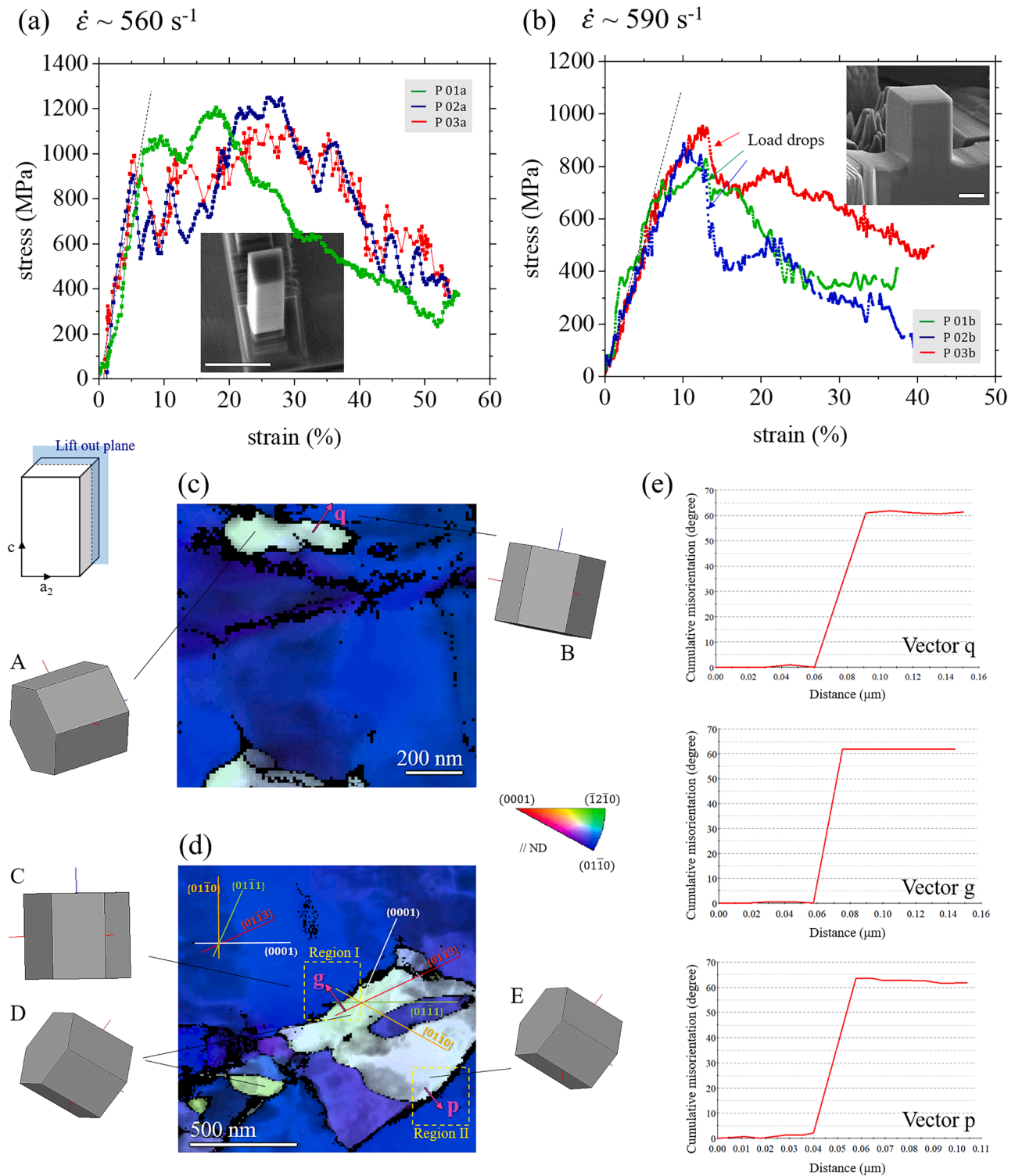
Fig. 6. Stress-strain curves and SPED orientation maps of [0001] shock-compressed pillars of different dimensions and aspect ratios: (a) 1.2×1.2 μm² (2:1 aspect ratio), (b) 5×5 μm² (3:2 aspect ratio). SEM images embedded in the graphs illustrate undeformed specimens. Scale bars: 2 μm. (c,d) Orientation maps obtained via SPED illustrating the formation of new grains in (c) 1.2×1.2 μm² (2:1 aspect ratio), and (d) 5×5 μm² (3:2 aspect ratio) pillars. The reliability index in the maps is greater than 20%, above the acceptability threshold. A graphic representation of the crystal orientations is reported to facilitate the visualization. The lift out plane is illustrated (the reference system corresponds to that of Fig. 1d). In (d), the (0001) -in white-, {10$\bar{1}$3} -in red-, {10$\bar{1}$1} -in green-, and {10$\bar{1}$0} -in orange- traces are highlighted within the parent and the new grain. (e) Cumulative misorientation profiles along the vectors indicated with **q**, **g** and **p** in (c,d). The new grains are characterized by a ~62° misorientation around the *a*-axis with respect to the initial crystal. The IPF colour code refers to the out-of-plane crystal direction (ND). (For interpretation of the references to colour in this figure legend, the reader is referred to the web version of this article.)

Table 2

Twin type and corresponding misorientation angle observed experimentally in the Mg crystal [2,30,46–50].

Type of twin	Misorientation angle/axis
$\{10\bar{1}1\}$	56.2° $<1\bar{2}10>$
$\{10\bar{1}2\}$	86.3° $<1\bar{2}10>$
$\{10\bar{1}3\}$	64° $<1\bar{2}10>$
$\{10\bar{1}4\}$	53° $<1\bar{2}10>$
$\{30\bar{3}2\}$	39.2° $<1\bar{2}10>$
$\{30\bar{3}4\}$	70.8° $<1\bar{2}10>$
$\{10\bar{1}1\}$-$\{10\bar{1}2\}$	37.5° $<1\bar{2}10>$
$\{10\bar{1}1\}$-$\{10\bar{1}2\}$	30.1° $<1\bar{2}10>$
$\{10\bar{1}1\}$-$\{10\bar{1}2\}$	66.5° $<5\text{-}943>$
$\{10\bar{1}1\}$-$\{10\bar{1}2\}$	69.9° $<2\text{-}421>$
$\{10\bar{1}2\}$-$\{10\bar{1}2\}$	7.4° $<1\bar{2}10>$
$\{10\bar{1}2\}$-$\{10\bar{1}2\}$	59.9° $<10\bar{1}0>$
$\{10\bar{1}2\}$-$\{10\bar{1}2\}$	60.4° $<\text{-}8170>$
$\{10\bar{1}2\}$-$\{10\bar{1}2\}$	22.2° $<1\bar{2}10>$

strain rates. Indeed, in the case of *c*-axis compression, the symmetry of the crystal with respect to the loading axis leads to twelve (six for $\{10\bar{1}1\}$ and six for $\{2\bar{1}\bar{1}2\}$) equivalently stressed pyramidal slip systems, which accommodate plastic deformation and promote the strong hardening observed in Fig. 4 up to 20% of strain. Nevertheless, in both cases the absence of twinning significantly reduces the ductility of Mg during *c*-axis compression and especially *c*-axis contraction. This is in contrast to *c*-axis extension experiments where deformation twinning represents the predominant mechanism that accommodates plastic deformation, allowing the material to withstand a large amounts of strain without cracking even at HSRs [44,45].

4.1. C-axis contraction: the case of the reoriented (44°, a-axis) grain

4.1.1. Hypothesis of $(0\bar{1}12)_m// (0001)_n$ weak twin

CTW or TTW do not contribute to accommodating plastic deformation in Mg during *c*-axis contraction. However, the nucleation of a new grain in Fig. 3f,g is observed and is likely induced by the high stress level achieved in the region indicated with letter "A" in the insert of Fig. 1a. "A" represents, due to the geometry of the specimen, the location of higher (triaxial) stress concentration. Therefore, complex strain fields can be perceived at the atomic scale, favouring the activation of equally complex deformation modes, especially upon exhaustion of dislocation-mediated plasticity. Although the nucleation of the new grain shown in Fig. 3f,g most likely occurred at high strain level and is therefore of very limited relevance to the mechanism of accommodation of the large imposed deformation (especially in relation to its limited spatial

evolution), it is nevertheless interesting to delve into its crystallographic characteristics. In particular, the 44° (±1°) matrix-new grain misorientation relationship between Grain 0 and Grain 1 (Fig. 3f,g) cannot be classified in terms of a known twinning system, predicted by the crystallographic shear-based theory of twinning [19] (Table 2). Other possibilities must therefore be considered.

It is to note that other matrix→new grain transformations that do not correspond to well-known twin systems have been recently observed. In particular, at high stress levels induced by either reducing the specimen size or under higher strain rate loading, the pyramidal I to basal plane transformation, reported to take place during [0001] compressions of Mg nanopillars [18], and the prismatic to basal plane transformation, that originates during [10$\bar{1}$0] compression [45,51–53], occur, suggesting that a deformation-induced plane transformation (unit cell reconstruction) has likely taken place in region A of Tb09 (Figs. 1a and 3f) under high loading rates. However, it is difficult to understand the precise mechanism that governed its nucleation. Contrary to the strain field exerted on the crystalline specimen under *c*-axis compression (expansion along the axes perpendicular to the *c*-axis), the strain field in *c*-axis contraction reduces the crystallographic *a*-axis compatibly to the orientation of the crystal relative to the loading direction (Fig. 1b). The atomic displacements corresponding to the mechanical loading are hence different from those in [0001] and [10$\bar{1}$0] compressions, and thus the prismatic to basal and pyramidal I to basal plane transformations cannot explain the (44°, *a*-axis) misorientation observed here.

Without restricting the investigation to classical twinning modes predicted by the crystallographic theory of twinning, to mathematically correlate the reorientation process of a crystal from an initial (matrix) *m* to a new *n* configuration, three matrices can be used [15]: the distortion matrix **F**, the coordinate transformation matrix **T**, and the correspondence matrix **C**, with **C** = **T F** (see Appendix A). Contrary to what is computed for deformation twinning, solutions that require the breakdown of the invariant plane strain condition were also considered here, which correlate the lattice of the matrix and the lattice of the new grain not necessarily by the same crystallographic plane (same Miller indices) or by two equivalent planes of the same family. This employs the concept of *weak twinning*. In relation to this, a possible solution emerged, for which the initial lattice is restored in a 43.1° reoriented new configuration around the *a*-axis (close to the values detected with EBSD). This (43.1°, *a*-axis) grain is given by:

$$\mathbf{F}_{hex} = \begin{pmatrix} 1 & 0.1235 & -0.6523 \\ 0 & 0.9135 & 0.3618 \\ 0 & 0 & 1.0945 \end{pmatrix} \qquad (2)$$
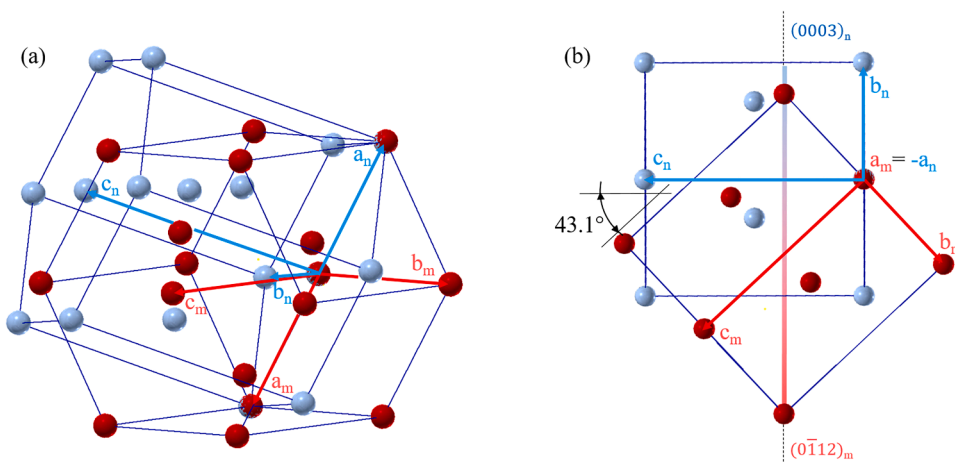

Fig. 7. Schematic representing the orientation relations between the parent and new grain crystals for the solution found in correspondence to the observed new grain formation in region A in Fig. 1a. (a) 43.1° misoriented parent (*m*, blue coloured) and new grain (*n*, red coloured) crystals around the *a*-axis. (b,c) $(0\bar{1}12)_m \rightarrow (0001)_n$ plane transformation. (b) represents the projection of the crystals viewed along the normal to the denoted planes. (For interpretation of the references to colour in this figure legend, the reader is referred to the web version of this article.)
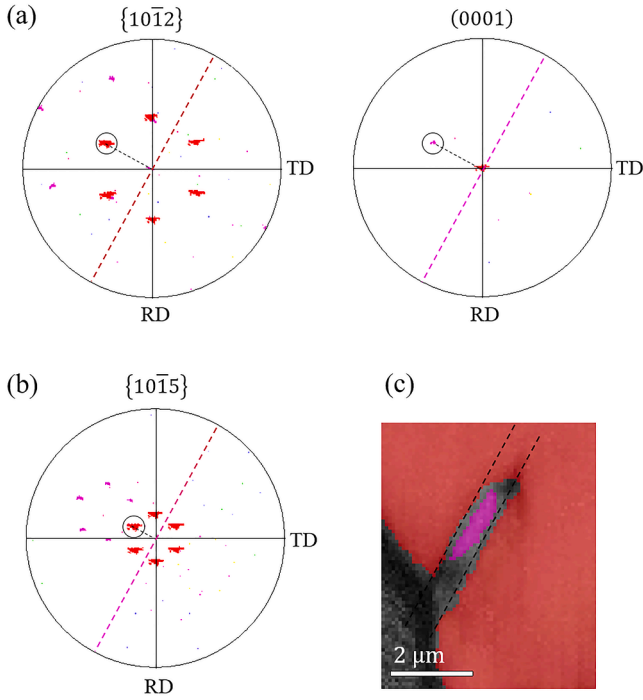
(a)

(b)

(c)

Fig. 8. Pole figures of the crystallographic planes that constitute the solution proposed to describe the grain formed in Tb09 (Fig. 3f,g). Colours refer to the IPF triangle of Fig. 3. The circles identify the overlapping stereographic projections of the normal of the parent and new grain planes that constitute the parent-new grain interface (Fig. 3g); the latter denoted with a dashed line. (b) Pole figure associated to the conventional $\{10\bar{1}5\}$ twin. (c) Interface between the initial and reoriented grains (replicated from Fig. 3g for reference).

$$\mathbf{T}^{n \to m}_{hex} = \begin{pmatrix} 1 & -0.1351 & 0.6407 \\ 0 & 0.7296 & 1.2814 \\ 0 & -0.3648 & 0.7296 \end{pmatrix} \tag{3}$$

from which

$$\mathbf{C}^{n \to m}_{hex} = \mathbf{T}^{n \to m}_{hex} \mathbf{F}_{hex} = \begin{pmatrix} 1 & 0 & 0 \\ 0 & 2/3 & 5/3 \\ 0 & -1/3 & 2/3 \end{pmatrix} \tag{4}$$

The details of the calculations are given in Appendix B. Concerning the solution found, using Eqs. (4) and (A.2) (Appendix A), the $(0\bar{1}12)_m$ plane ($(0\bar{1}2)$ in the 3-index notation) is transformed into the $(0003)_n$ plane (i.e. (001)). Accordingly, Grain 0 and Grain 1 (Fig. 3f) can be related by a $(0\bar{1}12)_m//(0001)_n$ *weak interface* (Fig. 7b–c). It is important to note that the trace of the interface experimentally observed (Fig. 3g) follows the dashed line reported in Fig. 8b. The relative pole figures marked by the circles shown in Fig. 8a indeed overlap. The 43.1° misorientation around the $[2\bar{1}\bar{1}0]$ axis (or a-axis) can be checked using the matrix of coordinate transformation between the parent and the new grain bases (Appendix A.2).

Interestingly, the obtained solution implies that a pyramidal II to basal plane transformation occurred, similarly to the pyramidal I to basal or prismatic to basal transformations reported elsewhere [18,51, 52]. The geometric parallelism between the basal plane in the new grain and the $(0\bar{1}12)$ pyramidal plane in the matrix is represented in Figs. 7c and B-1 (Appendix B). Note that for the described parent→new grain transformation, the distortion matrix does not correspond to that of a simple shear **S** typically used to describe the process of deformation twinning.

Using similar arguments as those introduced by Crocker and Bevis [47] to calculate the shear value s from the correspondence matrix in the case of simple shear, Cayron [54] proposed the alternative

generalization of s (called "generalized shear", s_g) that continues to work whatever the form of **F** (simple shear or not). s_g can be extracted from the distortion matrix **F** by

$$s_g^2 = Tr\left[\mathbf{G}(\mathbf{F} - \mathbf{I})\mathbf{G}^{-1}(\mathbf{F} - \mathbf{I})^T\right] \tag{5}$$

with **G** the metric tensor and **I** the 3×3 identity matrix. Eq. (5) is a generalization formula that encompasses the usual shear amplitude for simple shear distortions, and more generally, it allows to quantify the amplitude of any distortion. Other generalization formulae have also been proposed. Similarly to what was reported by Bevis and Crocker [55], Cayron [22] introduces the concept of "generalized strain" ε_g, expressed as:

$$\varepsilon_g^2 = Tr\left[\mathbf{G}\mathbf{F}\mathbf{G}^{-1}\mathbf{F}^T\right] - N \tag{6}$$

with N the dimension of the space ($N = 2$ in 2D, and $N = 3$ in 3D). (Note that for conventional twins: $s_g = \varepsilon_g = s$). For what concerns the case of pyramidal II/basal, (43°, a-axis), of interest here, $s_g = 0.595$ and $\varepsilon_g = 0.608$.

Yet, one may question why the pyramidal II/basal plane transformation has taken place compared to all the other possible *weak twins* that require lower generalized shear and strain amplitudes. An answer could be advanced by analyzing the schematic of the possible vector field of the overall atomic displacements occurring in the case of the $(0\bar{1}12)_m \to (0001)_n$ transformation. In Fig. B-2 (Appendix B), a proposed vector field appears coherent to the elastic strain field perceived by the unit cell at site "A" of the specimen in response to the externally applied load (Fig. 1a,b). This implies that changes in the direction of the locally perceived elastic strain field could limit the evolution of the new grain and explain why its growth does not cross the longitudinal axis of the T-bar (Fig. 3f). This is also to say that c-axis contraction conditions not produced in $[10\bar{1}0]$ micro-tensile loading would likely not result in the formation of the same grain observed here. Even though this reasoning is simply in line with the necessary affinity between required atomic displacements for new grain nucleation/propagation and externally applied strain field, which seems to govern the selection of new grains (*weak twins*) and affect their consequent growth, it still represents a premature conclusion. Indeed, the stress state ahead of the twin tip could be extremely singular [44,56–58] and more *in situ* information at that location would be required, leaving space to further future investigations.

4.1.2. Hypothesis of high index $\{10\bar{1}5\}$ conventional twin

A correlation can also be found between the pyramidal II/basal *weak twin* and a conventional type I twin mode: the $\{10\bar{1}5\}$ twin. Such a high index twin has never been reported so far, it is characterized by a 41° misorientation around the a-axis, with its correspondence matrix exactly that of Eq. (4), as it maintains the $(0\bar{1}15)$ unchanged (see Appendix B), its shear value equal to 0.608, and its plane trace follows that of the experimentally observed interface (Fig. 8b,c). Using the mathematical approach adopted in [21,23] for TTW and CTW, the distortion matrix $\mathbf{F}^{0\bar{1}15}_{hex}$ associated to the $\{10\bar{1}5\}$ twin can be derived by applying a small angular correction of 2.1° around the a-axis, as:

$$\mathbf{F}^{0\bar{1}15}_{hex} = \mathbf{R}^{2.1°}_{hex} \mathbf{F}_{hex} = \begin{pmatrix} 1 & 0.1235 & -0.6523 \\ 0 & 0.9129 & 0.4027 \\ 0 & -0.0343 & 1.0801 \end{pmatrix} \tag{7}$$

Differently to **F**, $\mathbf{F}^{0\bar{1}15}_{hex}$ is a simple shear matrix. The set of eigenvalues is reduced to {1} and its eigenspace is of dimension 2, formed by the vectors [100] and [051] (expressed in the three-index notation), i.e. the $(0\bar{1}5)$ plane. The shear vector, as well as its amplitude, can be determined in the orthonormal basis by:
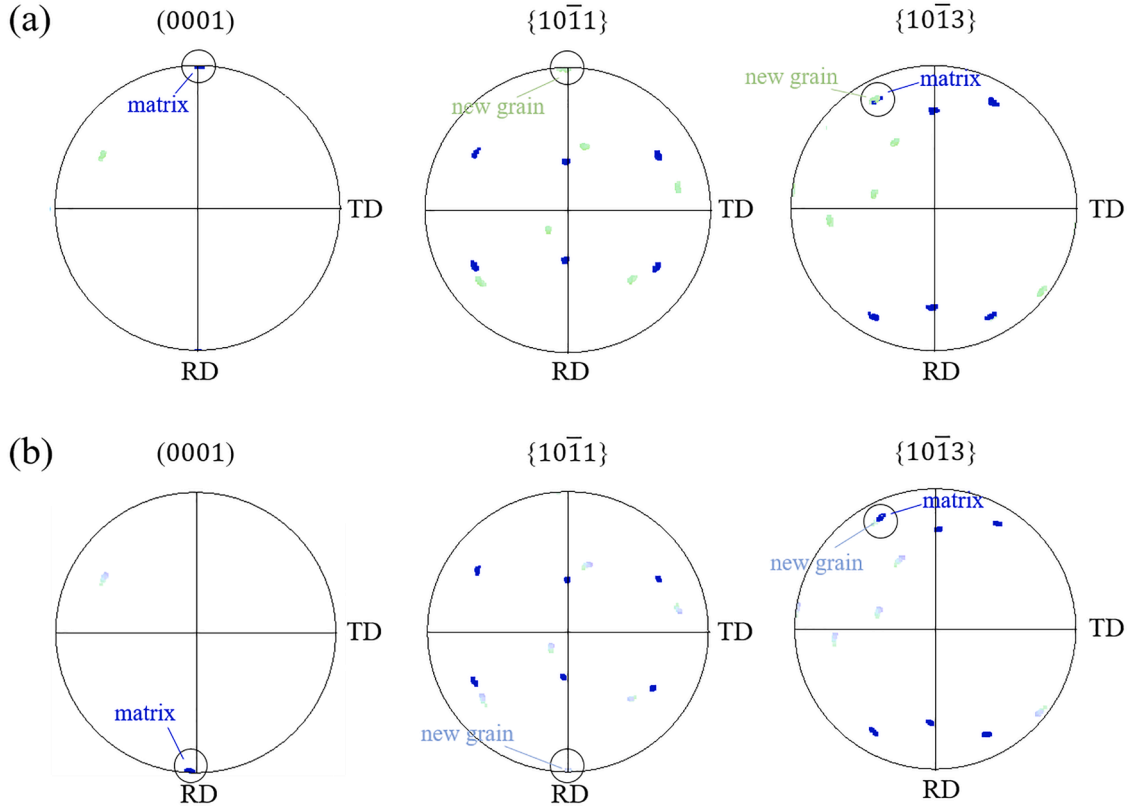
Fig. 9. (0001), $\{10\bar{1}1\}$ and $\{10\bar{1}3\}$ pole figures illustrating the two different solutions that can describe the character of the parent-new grain interfaces formed in [0001] compressed micropillars (Fig. 6c,d). Colours refer to the invers pole figure of Fig. 6. The pole figures in (a) are taken from the sub-region I shown in Fig. 6d whilst those in (b) from sub-region II. The circles identify the overlapping stereographic projections of the normal of the parent and new grain planes that constitute the parent-new grain interface.
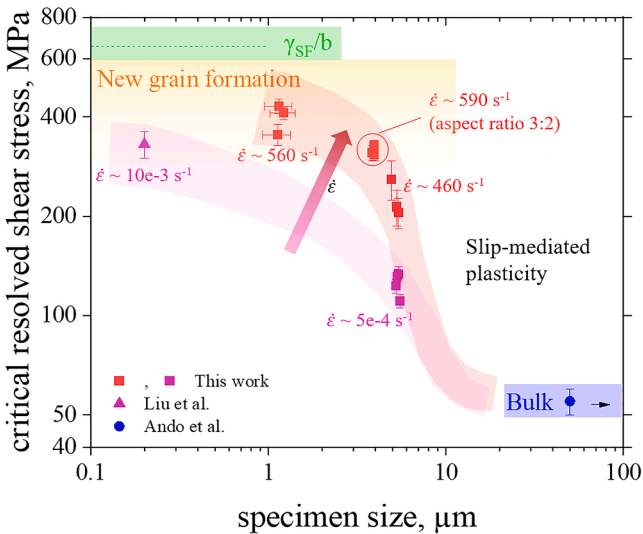
Fig. 10. Critical resolved shear stress (calculated at the yield point) of Mg micropillars oriented to deform by pyramidal slip as a function of strain rate and specimen size. Data refer to pillars with aspect ratio of 2:1, unless specified otherwise. Data point for Liu et al. and Ando et al. are taken from [18,62]. Note that the value of CRSS from Ando et al. refers to bulk Mg, and thus does not fall within the range of specimen size illustrated in the figure. The deformation mechanism map is shown by coloured regions. Note: stacking fault energy of pyramidal slip is considered ca. 425 ± 25 mJ m^{-2} from [63]; $b_{<c+a>} = 0.612$ nm.

$$\mathbf{s} = \left(\mathbf{F}_{ortho}^{0\bar{1}15} - \mathbf{I}\right) \cdot \mathbf{n}_{ortho} = \begin{pmatrix} -2.59 \\ 1.0715 \\ 0.4515 \end{pmatrix} \qquad (8)$$

where $\mathbf{n}$, expressed in the orthonormal basis in Eq. (8), represents the vector normal to the $(0\bar{1}5)$ plane, i.e.

$$\mathbf{n}_{ortho} = \begin{bmatrix} 0 & -\gamma & 5\dfrac{\sqrt{3}}{2} \end{bmatrix} \qquad (9)$$

with $\gamma = c/a$ (ratio of lattice parameters; 1.624 for Mg). The shear amplitude is therefore

$$s = \frac{\mathbf{s}}{\mathbf{n}} \approx 0.608 \qquad (10)$$

It is equal to the "generalized strain" ε_g of the $(0\bar{1}12)_m // (0001)_n$ weak twin described in the previous section. This value of shear is relatively high compared to that required for other possible twinning modes in Mg. Nevertheless, considering that deformation twins in face centered cubic metals, as well as in twinning-induced plasticity steels, are (111) <112> with a shear amplitude of 0.7, the solution proposed here may be equally realistic. The hcp unit cell reconstruction through pyramidal II to basal plane transformation could be therefore the "sister" of the $\{10\bar{1}5\}$ classical simple shear twin. Unfortunately, the two hypotheses (weak twin or high index type I twin) could not be distinguished from the trace visible in Fig. 8, and no 3D reconstruction could be done. Further considerations of the relation between weak twins and conventional twins are reported in Appendix C.

4.2. C-axis compression: the case of the reoriented (62°, a-axis) grain

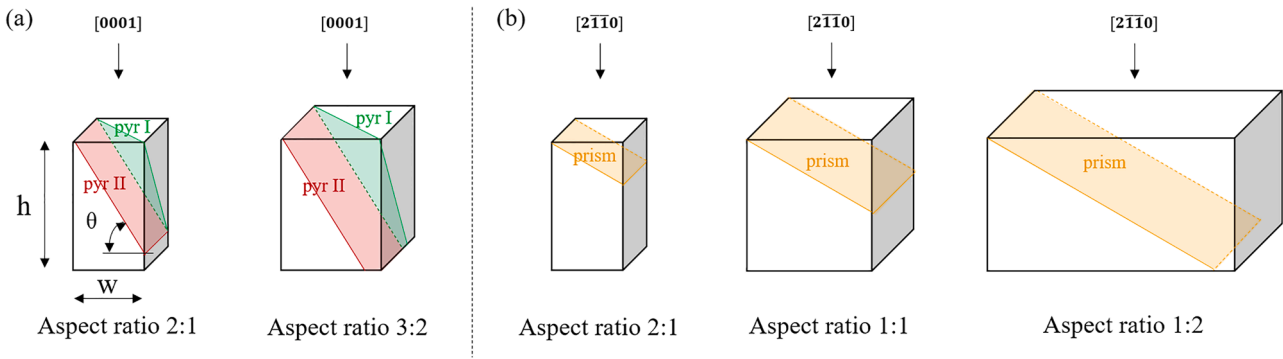The formation of new grains was also observed in *c*-axis compression

Fig. 11. Schematic of the geometrical relationships between the traces of the active slip modes and the pillar aspect ratio during (a) [0001] and (b) [2$\overline{1}\overline{1}$0] compressions. The impossibility for the preferable deformation slip mode to cross the specimen from one side to the other occurs in specimens where the aspect ratio becomes lower than tan(θ). θ is defined as the angle between the sliding plane and the horizontal plane.
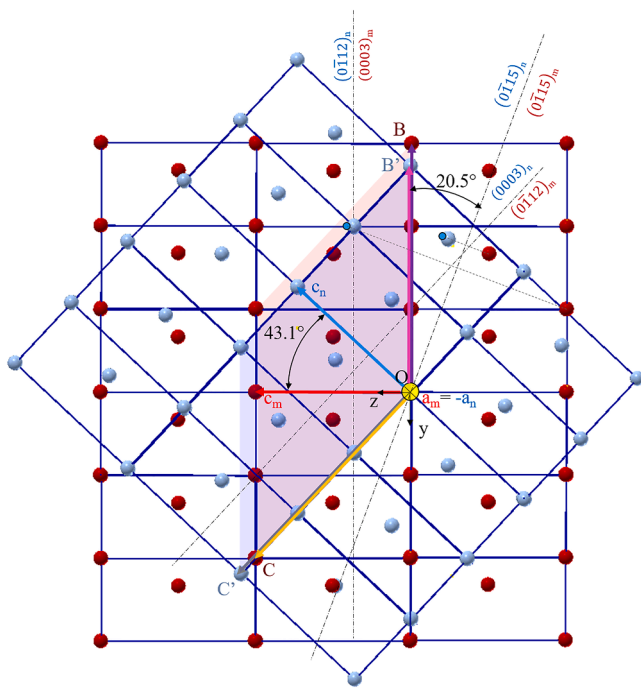

Fig. B 1. Model of (0$\overline{1}$12)→(0003) transformation. Series of unit cell repeated periodically and viewed in projection perpendicularly to the a-axis. The new grain appears blue, the parent grain in red. The rotation axis is indicated by the yellow coloured circle, representing also the origin of the orthogonal and hexagonal bases. Vectors OA and OB are perpendicular and parallel to the plane of view, respectively. The parent→new grain transformation converts the (0$\overline{1}$12)$_m$ into the (0003)$_n$, and the (0003)$_m$ into the (0$\overline{1}$12)$_n$. The final configuration is very close to the exact mirror symmetry across the (0$\overline{1}$15) plane. The atomic positions of the new grain are very close to the positions that would be obtained by mirror symmetry across the (0$\overline{1}$15) plane, as indicated by the black dashed lines perpendicular to the (0$\overline{1}$15) plane, as well as by the small blue circles. Atoms in A, B and C, constitute the ABC supercell (transparent red); atoms in A', B', and C', constitute the distorted ABC supercell (transparent blue), i.e. (ABC)'.

(Fig. 6). Here, the parent-new grain misorientations mostly correspond to ~62° around the a-axis, recently reported to be produced by the {10$\overline{1}$1}$_m$→(0001)$_n$ (pyramidal I→basal) plane transformation [18]. (Supp Fig. S-2 contains a more complete list of the orientation relationships between the different grains observed in Fig. 6d). It should be observed that the rarely operative {10$\overline{1}$3} CTW in Mg, predicted by the crystallographic shear-based theory of twinning, is also

characterized by a 64° misorientation around the a-axis (see Table 2) [30]. For completeness, Fig. 9 reports the pole figures associated to the (0001), {10$\overline{1}$1} and {10$\overline{1}$3} families of planes. By comparing Figs. 9 and 6c,d, it appears that the traces of the grain boundaries agree with both the {10$\overline{1}$3} conventional twin and the (0001)//{10$\overline{1}$1} weak twin. An explanation of this can be found in Appendix C. From the perspective of the material response, a large strain burst marks the nucleation of new grains in the nanopillars compressed by Liu et al. [18], in load-controlled testing mode. In displacement-controlled testing mode, employed in the present study, their nucleation likely corresponds to the load drops observed in Fig. 6a,b, not observed in Fig. 4a–d. Nevertheless, it is important to understand why, during [0001] compressions, the formation of weak twins occurs in submicron-size [18] rather than micron-size pillars with aspect ratio of 2:1, or in micron-size pillars by lowering the aspect ratio.

4.2.1. Smaller pillar cross-section, same aspect ratio

The formation of new grains in smaller pillars can be explained in terms of size-dependent plasticity [59,60]. In contrast to the occurrence of massive shearing produced by single deformation slip crossing the entire specimen, single-ended source length dislocations form in pillars of smaller volumes as a result of truncation of dislocation source operation by free surfaces and justify the sample size effect on the measured flow stress of microcrystals [59]. In particular, below a critical size, the statistical averaged distance between the dislocation pin and the free surface becomes too small, which requires a higher force to operate pre-existing dislocations via Orowan bowing mechanism [61], eventually leading to the conversion from a propagation to a nucleation-limited dislocation mechanism. The strain rate-dependent balance between the rate of heterogeneous dislocation nucleation from free surfaces and the rate of dislocation escape at free surfaces (before being able to multiply), defines the dislocation density within the pillar volume during the deformation. The plastic flow thus differs from the continuous strain hardening of bulk crystals, inducing changes in the deformation mechanism behavior. In particular, the material is initially forced to withstand a large part of the deformation by thickening the specimen along the direction perpendicular to the direction of the load (barrelling). In this regards, in the work of Liu et al. [18] it is indeed clear from *in situ* TEM compressions that all the nanospecimens undergo a barreling mechanism throughout the deformation rather than exhibiting the visible sliding along crystallographic slip planes observed in the micron-size pillars (5 × 5 μm^2 and 2:1 aspect ratio, Figs. 4 and 5). In turn, the high multi-axial stress condition that accumulates within their pillars, induces the (10$\overline{1}$1)$_m$→(0001)$_n$ plane transformation, i.e. the new grain formation. Similarly to that, the high stress levels achieved here by imposing high deformation-rates to ~1.2 μm sized pillars (also ~1 GPa - Fig. 6b), kinetically delays the time interval within which the deformation is accepted by shearing along crystallographic slip planes,
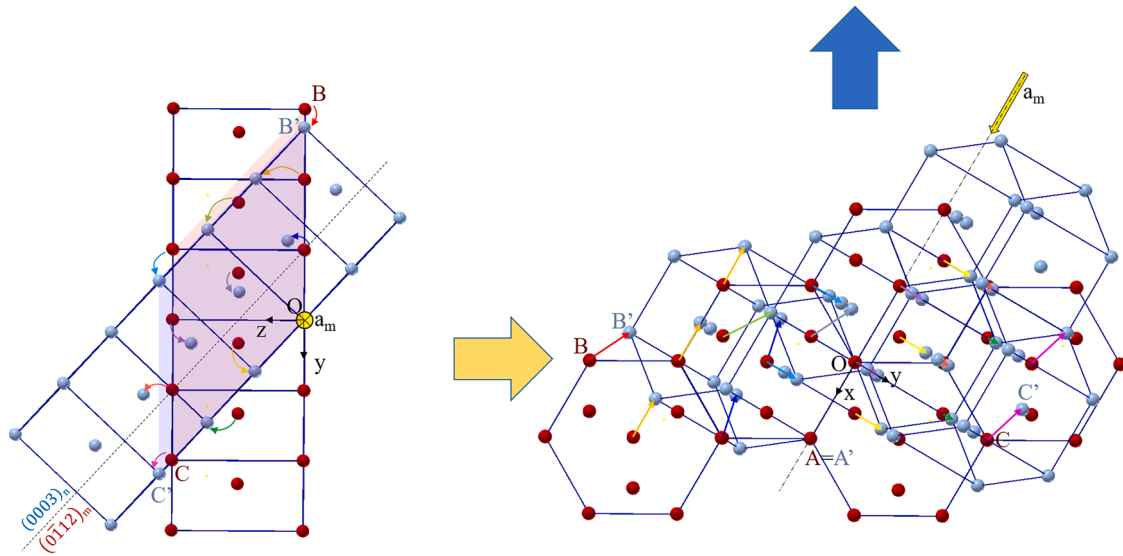
Fig. B 2. Proposition of atom displacements for the $(0\bar{1}12)\rightarrow(0003)$ transformation, close to the exact mirror symmetry across the $(0\bar{1}15)$ plane. For the former, the matrix (red) and new hcp unit cell (blue) have a 43.1° $<2\bar{1}\bar{1}0>$ misorientation; for the latter, they have a 41° $<2\bar{1}\bar{1}0>$ misorientation. The locally perceived strain field in the region "A" of the material (Fig. 1a) is indicated by the two bigger arrows on the right-hand side. The vector field of atomic displacements that induces the $(0\bar{1}12)_m\rightarrow(0001)_n$ plane transformation is illustrated by differently coloured arrows. Note that the atomic displacements have almost the same magnitude and are pertinent to the external stress field. The distortion is calculated by considering only the displacements of the atoms in A, B and C, constituting the ABC supercell. It is assumed that their motion causes the subsequent atomic repositioning of the other atoms, similar to a knock-on effect. We cannot prove that this filed of atomic displacements gives the best solution for this transformation.

causing the formation of the detected new grains (Fig. 6c). On this basis, it appears that a high stress state represents the necessary requirement to obtain the activation condition for weak twinning (Fig. 10). In support of this consideration, also the prismatic→basal plane transformation (leading to 90° misoriented grains with respect to the parent crystal around the *a*-axis) has been reported to occur under high-stress conditions obtained either by reducing the size [52] or by increasing strain rate [45,53].

4.2.2. Same pillar cross-section, smaller aspect ratio

A reduction in the aspect ratio of the specimen from 2:1 to 3:2 (while keeping same dimensions: 5×5 μm^2) has also been observed to induce the formation of new grains (Fig. 6b,d). The main effect of reducing the aspect ratio resides in the change of the geometrical constraints exerted by the surrounding material that yield a deformation behaviour for which the material is forced to barrel. In other words, the initial barreling-induced high multi-axial deformation state may be caused by the geometrical impossibility for the preferable deformation slip mode to cross the specimen from one side to the other (Fig. 11a). Indeed, setting (90-θ) the angle between the loading direction and the slip plane with the highest Schmid factor, it is reasonable that barreling is favored in specimens with aspect ratio $<$ tan(θ), limiting the rate of dislocation escape by crossing the specimen with consequent development of high internal stresses and dislocation density. In addition to that, by reducing the aspect ratio, the diagonal shear bands that form at the top edges of the pillar intersect at the bulk volume below the specimen and further produce a high local triaxial stress state, promoting the occurrence of complex deformation mechanisms. Along this line, Sim et al. [64] report molecular dynamic (MD) simulations that reveal the evolution of the deformation microspecimen in Mg pillars of different aspect ratios oriented with the $[2\bar{1}\bar{1}0]$ direction parallel to the loading direction (Fig. 11b). In their work, even if not clearly addressed, the decrease in aspect ratio to 1:2 (height vs width) leads to the impossibility of prismatic slip to cross the specimen, causing a higher amount of dislocations to remain confined within the pillar volume with a subsequent formation of a new grain 90° misoriented with respect to the parent crystal. Such formation of a new grain was not observed in their work in

specimens with higher aspect ratio, and can be extended to the present work.

5. Summary and conclusions

In this work, the mechanical response of pure magnesium under *c*-axis compression and contraction has been investigated at the microscale, extending the currently published results to high strain rate deformations. In line with what was observed elsewhere [5–7], the accommodation of the plastic deformation occurs predominantly by pyramidal and prismatic slip during *c*-axis compression and contraction, respectively. The strain rate sensitivities associated to these deformation modes were found to be similar and in the range from 0.01 to 0.131. The increase in the stress induced by the increase in strain rate, however, has not triggered the activation of CTW within the specimens in both the loading modes. Nevertheless, at high strain rates, new grains have been detected, whose crystallographic characteristic could be attributed to either specific unconventional twins (*weak twins* [22]) or conventional twins (i.e. predicted by the classical shear-based theory of twinning) that underwent a small angular distortion of ~2°. To raise awareness of the relevance of the experimental observation of new grains, it is worth to remind that several other works report "anomalous" twinning characteristics [11,65] such as twins whose habit planes are not invariant. As any theory should be judged by its predictions, the increasing number of experimental evidence of unusual misorientation relationships that cannot be related to known twinning systems suggests that the formation of new grains in Mg, and the mechanism governing the incubation period of an embryonic twin, cannot be treated through the shear-based theory of twinning (i.e. distortion matrix being a shear matrix). The concept of *weak twinning* [22], was therefore adopted in this work, in which the parent-new grain interface is not anymore necessarily fully invariant as for usual deformation twinning, but can be slightly distorted to be transformed into a new non-equivalent plane. This approach revisits the list of possible lattice transformations and allowed to identify a pyramidal II to basal plane transformation during c-axis contraction for which the required field of atomic displacements appears pertinent to the strain field perceived by the material at the nucleation site. Grains

with crystallographic features suggesting a mechanism of unit cell reconstruction through the transformation from pyramidal I to basal plane were also observed in c-axis compression, in line with recent published work [18]. Nevertheless, the increase in pillar size and in aspect ratio seems to disfavour the formation of new grains. As the new grain formation represents an alternative to cracking, the choice of the pillar size in micro specimens may represent a strategy to adapt the plasticity for a given strain level, enhancing the ductility of Mg. Indeed, due to the crystal reorientation, the formation of these new grains promotes the activation other deformation modes (slip and twinning) within them, improving the machinability of Mg and its alloys. In particular, the disfavored activation of the easy basal slip mode in the parent crystal, for the imposed loading conditions, becomes favorable upon reorientation [18]. On the other hand, however, the complex new grain morphology induced by the inhomogeneous deformation associated with the formation of unconventional twin interfaces, may result in localization of plastic deformation and consequent failure. Nevertheless, when gliding planes are nearly parallel between two neighboring misoriented grains (as in the case of "*weak twin*" interfaces), slip transmission across these boundaries may result easier; stress concentrations at twin boundary–slip interaction sites could be easily relieved, limiting pile-up stresses, multiple twin nucleation events and formation of cracks.

Finally yet importantly, due to the high stress level required for new grain formation in these loading conditions, it can be questioned to which extent the mechanism of new grain formation can be applied in bulk Mg. High stress conditions can be achieved at the grain boundaries, vicinity of precipitates, and in front of dislocation pile-ups, suggesting that it might be also detected in bulk polycrystalline samples. However, it could not be potentially generalized as a main mechanism of deformation as it requires exceptionally high stresses and specific strain fields for a precise crystallographic orientation, and the material may likely fail before new grain formation occurs. To the best of the authors' knowledge, the nucleation of the observed new grains has not been reported in bulk magnesium single crystals compressed along the c-axis at room temperature.

Data availability

The data that support the findings of this study are available from the corresponding author upon reasonable request.

Declaration of Competing Interest

The authors declare no competing interests.

Supplementary materials

Supplementary material associated with this article can be found, in the online version, at doi:10.1016/j.actamat.2023.118762.

Appendices

Transformation matrices

As reported in the main text, to mathematically correlate the reorientation process of a crystal from an initial (matrix) *m* to a new *n* configuration, three matrices can be used [15]: the distortion matrix **F**, the coordinate transformation matrix **T**, and the correspondence matrix **C**, with **C** = **T F**. **F** can be calculated in practice considering the vectors of the initial (matrix) basis ($\mathbf{a}_{1m}$, $\mathbf{a}_{2m}$, $\mathbf{c}_m$) transformed by the distortion into new vectors: $\mathbf{a}_{1m} \to \mathbf{a'}_{1m}$, $\mathbf{a}_{2m} \to \mathbf{a'}_{2m}$ and $\mathbf{c}_m \to \mathbf{c'}_m$. In other words, the distortion matrix **F** is the matrix formed by the images $\mathbf{a'}_{1m}$, $\mathbf{a'}_{2m}$ and $\mathbf{c'}_m$ expressed in the initial hexagonal basis (B_{hex}^m): i.e. $\mathbf{F} = (\mathbf{a'}_{1m},\ \mathbf{a'}_{2m},\ \mathbf{c'}_m)_{/B_{\text{hex}}^m}$. **T** is determined from the orientational relationship between the parent and the new reoriented grain, experimentally obtained from the EBSD measurements. The condition that the parent and the new grain have the same volume ensures that **F, T** and **C** are unimodular, i.e. have determinants of ± 1. A further mathematical restriction is that the transformation matrix should fulfil $\mathbf{T} \cdot \mathbf{T}^{\mathbf{T}} = \mathbf{I}$.

A.1 The use of the correspondence matrix

If **r** represents a generic vector written in the initial basis (B_{hex}^m), knowledge of the correspondence matrix $\mathbf{C}_{hex}^{n \to m}$ is useful to express in the new grain basis (B_{hex}^n) the coordinates of **r'** (i.e. **r** after the distortion) as follows:

$$\mathbf{r'}_{\mathbf{B}_{hex}^n} = \mathbf{C}_{hex}^{n \to m}\ \mathbf{r}_{\mathbf{B}_{hex}^m} \tag{A.1}$$

Considering **r** the vector normal to the crystallographic plane **J** (defined by the Miller indices *h, k, l*, when expressed in the 3-index notation), **r*** in reciprocal space is then a vector whose components are *h, k, l*. Thus,

$$\mathbf{r}_{J/\mathbf{B}_{hex}^n}^{*\,'} \;=\; \left(\mathbf{C}_{hex}^{n\to m}\right)^{*} \mathbf{r}_{J/\mathbf{B}_{hex}^m}^{*} = \left(\mathbf{C}_{hex}^{n\to m}\right)^{-T} \mathbf{r}_{J/\mathbf{B}_{hex}^m}^{*} \tag{A.2}$$

where

$$\left(\mathbf{C}_{hex}^{n\to m}\right)^{*} \;=\; \left(\mathbf{C}_{hex}^{m\to n}\right)^{T} \tag{A.3}$$

A.2 The use of the coordinate transformation matrix

It is noted that matrices equivalent to $\mathbf{T}_{hex}^{n\to m}$ can be obtained by multiplying $\mathbf{T}_{hex}^{n\to m}$ by the matrices of internal symmetry $\mathbf{M}$ of the hexagonal phase (matrices forming the point group of the hcp phase [66]). For example, in order to determine the rotation matrix $\mathbf{R}_{ortho}^{n\to m}$ expressed in an initial orthogonal basis ($\mathbf{B}_{ortho}^m$), which in turn is related to the hexagonal basis ($\mathbf{B}_{hex}^m$) by

$$\mathbf{H}_{hex} = \left[\mathbf{B}_{ortho}^m \to \mathbf{B}_{hex}^m\right] = \begin{pmatrix} 1 & -\dfrac{1}{2} & 0 \\ 0 & \dfrac{\sqrt{3}}{2} & 0 \\ 0 & 0 & \gamma \end{pmatrix} \tag{A.4}$$

with $\gamma = c/a$ (ratio of lattice parameters), the matrix $\mathbf{T}_{hex}^{n\to m}$ can be composed with the mirror symmetry $\mathbf{M}_{hex}$ and then be expressed in $\mathbf{B}_{ortho}^m$. Taking for example the coordinate transformation matrix of Eq. (3) in the main text, the result will be:

$$\mathbf{R}_{ortho}^{n\to m} \;=\; \mathbf{H}_{hex}\mathbf{M}_{hex}\mathbf{T}_{hex}^{n\to m}\,\mathbf{H}_{hex}^{-1} = \begin{pmatrix} -1 & 0 & 0 \\ 0 & 0.7296 & 0.6835 \\ 0 & 0.6839 & -0.7296 \end{pmatrix} \tag{A.5}$$

with

$$\mathbf{M}_{hex} \;=\; \begin{pmatrix} -1 & 1 & 0 \\ 0 & 1 & 0 \\ 0 & 0 & -1 \end{pmatrix} \tag{A.6}$$

The matrix $\mathbf{R}_{ortho}^{n\to m}$ represents a rotation around the a-axis of angle $\cos^{-1}(0.7296) = 43.1°$.

B. Pyramidal II → basal plane transformation: correspondence, distortion and transformation matrices calculation

We have imagined, after many unproductive attempts, a vector field of atomic displacements that represents the pyramidal II (parent, or matrix m) to basal (new grain, n) plane transformation. Although we cannot ascertain that this model gives the best solution, the solution that emerges provides a series of atomic movements that seem reasonable because are coherent with the strain field perceived in location A (Fig. B-1a), they are small and restore the hcp lattice at the end of the process.

We define $\mathbf{B}_{hex} = (a, b, c)$ the usual hexagonal basis and $\mathbf{B}_{ortho} = (x, y, z)$ the orthonormal basis represented in Fig. B-1 and linked to $\mathbf{B}_{hex}$ by the coordinate transformation matrix $\mathbf{H}_{hex}$ reported in Eq. (A.4).

The distortion matrix can be calculated by considering an appropriate supercell that conserves the volume at the end of the process. In the present case, the unit cell is ABC (Figs. B-1 and B-2). The three column vectors of this cell, OA, OB and OC, form a basis $\mathbf{B}_{ABC}$ given in $\mathbf{B}_{ortho}$ by the coordinate transformation matrix:

$$\left[\mathbf{B}_{ortho}\to\mathbf{B}_{ABC}\right] = \mathbf{B}_{ABC} = \begin{pmatrix} 1 & 3/2 & -1 \\ 0 & -3\dfrac{\sqrt{3}}{2} & \sqrt{3} \\ 0 & 0 & \gamma \end{pmatrix} \tag{B.1}$$

The three column vectors of the deformed supercell (when the transformation is completed), OA', OB' and OC', form a basis $\mathbf{B}_{(ABC)'}$ given in $\mathbf{B}_{ortho}$ by the coordinate transformation matrix:

$$\left[\mathbf{B}_{ortho}\to\mathbf{B}_{(ABC)'}\right] = \mathbf{B}_{(ABC)'} = \begin{pmatrix} 1 & 1 & -\dfrac{1}{2} \\ 0 & -2.373 & 1.9066 \\ 0 & 0 & 1.7625 \end{pmatrix} \tag{B.2}$$

The distortion matrix of the process is given in the basis $\mathbf{B}_{ortho}$ by the matrix $\mathbf{F}_{ortho}$:

$$\mathbf{F}_{ortho} = \mathbf{B}_{(ABC)'}\left(\mathbf{B}_{ABC}\right)^{-1} \;=\; \begin{pmatrix} 1 & 0.1924 & -0.5132 \\ 0 & 0.9136 & 0.1996 \\ 0 & 0 & 1.0945 \end{pmatrix} \tag{B.3}$$

The determinant of the matrix is 1, confirming that the ABC and (ABC)' supercells have the same volume.
This matrix can be expressed in the hexagonal basis $\mathbf{B}_{hex}$ by using the formula of coordinate change:

$$\mathbf{F}_{hex} = (\mathbf{H}_{hex})^{-1}\mathbf{F}_{ortho}\mathbf{H}_{hex} = \begin{pmatrix} 1 & 0.1235 & -0.6523 \\ 0 & 0.9135 & 0.3618 \\ 0 & 0 & 1.0945 \end{pmatrix} \tag{B.4}$$

which reflects that of Eq. (2). Note that the displacement field is given by:

$$\mathbf{x}'_{/\mathbf{B}^m_{hex}} - \mathbf{x}_{/\mathbf{B}^m_{hex}} = (\mathbf{F}_{hex} - \mathbf{I}) \cdot \mathbf{x}_{/\mathbf{B}^m_{hex}} \tag{B.5}$$

where $\mathbf{x}$ is a vector of the parent basis that defines the initial atomic positions, and $\mathbf{x}'$ is the image of a vector $\mathbf{x}$ obtained by a linear distortion: $\mathbf{x}'_{/\mathbf{B}^m_{hex}} = \mathbf{F}_{hex} \cdot \mathbf{x}_{/\mathbf{B}^m_{hex}}$.

Despite $\mathbf{F}_{hex}$ is calculated by considering only the displacements of the atoms in A, B and C, it is assumed that their motion causes the subsequent atomic repositioning of the other atoms, similar to a knock-on effect.

The correspondence matrix, nevertheless, can be calculated by considering the vectors used to build the ABC cell:

$$\mathbf{OA} : \mathbf{a}_m \rightarrow \mathbf{OA} : \mathbf{a}_m = -\mathbf{a}_n$$

$$\mathbf{OB} : -3\mathbf{b}_m \rightarrow \mathbf{OB} : -3\mathbf{b}_m = 2\mathbf{b}_n + \mathbf{c}_n$$

$$\mathbf{OC} : 2\mathbf{b}_m + \mathbf{c}_m \rightarrow \mathbf{OC} : (2\mathbf{b}_m + \mathbf{c}_m) = -3\mathbf{b}_n \tag{B.6}$$

where: $\mathbf{a}_m$ is along x, $\mathbf{b}_m$ along $y, -\frac{1}{2}x$ and $\mathbf{c}_m$ along z.

This means that the basis $\mathbf{B}^m_{ABC}$ formed by the three vectors $\mathbf{a}_m, -3\mathbf{b}_m, and 2\mathbf{b}_m + \mathbf{c}_m$, written as a column, is transformed by distortion into a matrix formed by three new vectors equal to $-\mathbf{a}_n, 2\mathbf{b}_n + \mathbf{c}_n, and -3\mathbf{b}_n$, of the twinned crystal. They form a new basis noted $\mathbf{B}^n_{(ABC)'}$. The negative sign of $-\mathbf{a}_n$ is a direct consequent of having imposed the condition that both have a positive determinant. The basis $\mathbf{B}^m_{ABC}$ expressed in the parent basis $B_h e x^m = (am, bm, cm)$ and the basis $\mathbf{B}^n_{(ABC)'}$ expressed in the new grain basis $B_h e x^n = (an, bn, cn)$ are, respectively, given by:

$$\mathbf{B}^m_{ABC} = \begin{pmatrix} 1 & 0 & 0 \\ 0 & -3 & 2 \\ 0 & 0 & 1 \end{pmatrix} \tag{B.7}$$

$$\mathbf{B}^n_{(ABC)'} = \begin{pmatrix} -1 & 0 & 0 \\ 0 & 2 & -3 \\ 0 & 1 & 0 \end{pmatrix} \tag{B.8}$$

$\mathbf{T}^{m \rightarrow n}_{hex}$ represents the coordinate transformation matrix from the parent to the new crystal. The basis $\mathbf{B}^n_{(ABC)'}$ expressed in the basis $\mathbf{B}^m_{hex}$ is $\mathbf{B}^m_{(ABC)'} = \mathbf{T}^{m \rightarrow n}_{hex}\mathbf{B}^n_{(ABC)'}$. Therefore:

$$\mathbf{F}_{hex}\mathbf{B}^m_{ABC} = \mathbf{T}^{m \rightarrow n}_{hex}\mathbf{B}^n_{(ABC)'} \tag{B.9}$$

or, equivalently:

$$\mathbf{F}_{hex}\left(\mathbf{C}^{n \rightarrow m}_{hex}\right)^{-1} = \mathbf{T}^{m \rightarrow n}_{hex} \tag{B.10}$$

where

$$\mathbf{C}^{n \rightarrow m}_{hex} = \mathbf{B}^n_{(ABC)'}\left(\mathbf{B}^m_{ABC}\right)^{-1} \tag{B.11}$$

For further information about the general formulæ refer to Ref. [23].

The calculation leads to:

$$\mathbf{C}^{n \rightarrow m}_{hex} = \begin{pmatrix} -1 & 0 & 0 \\ 0 & -2/3 & -5/3 \\ 0 & -1/3 & 2/3 \end{pmatrix} \tag{B.12}$$

$$\mathbf{T}^{n \rightarrow m}_{hex} = \begin{pmatrix} -1 & 0.1351 & -0.6407 \\ 0 & -0.7296 & -1.2814 \\ 0 & -0.3648 & 0.7296 \end{pmatrix} \tag{B.13}$$

We remind that matrices equivalent to $\mathbf{T}^{n \rightarrow m}_{hex}$ and $\mathbf{C}^{n \rightarrow m}_{hex}$ can be obtained by multiplying $\mathbf{T}^{n \rightarrow m}_{hex}$ and $\mathbf{C}^{n \rightarrow m}_{hex}$ by the matrices of internal symmetry $\mathbf{M}_{hex}$ of the hexagonal phase (matrices forming the point group of the hcp phase [66]). In other words:

$$\mathbf{C}^{n \rightarrow m}_{hex} = \mathbf{M}_{hex}\mathbf{C}^{n \rightarrow m}_{hex} = \begin{pmatrix} -1 & 0 & 0 \\ 0 & -1 & 0 \\ 0 & 0 & 1 \end{pmatrix}\begin{pmatrix} -1 & 0 & 0 \\ 0 & -2/3 & -5/3 \\ 0 & -1/3 & 2/3 \end{pmatrix} = \begin{pmatrix} 1 & 0 & 0 \\ 0 & 2/3 & 5/3 \\ 0 & -1/3 & 2/3 \end{pmatrix} \tag{B.14}$$

$$\mathbf{T}^{n \rightarrow m}_{hex} = \mathbf{M}_{hex}\mathbf{T}^{n \rightarrow m}_{hex} = \begin{pmatrix} -1 & 0 & 0 \\ 0 & -1 & 0 \\ 0 & 0 & 1 \end{pmatrix}\begin{pmatrix} -1 & 0.1351 & -0.6407 \\ 0 & -0.7296 & -1.2814 \\ 0 & -0.3648 & 0.7296 \end{pmatrix} = \begin{pmatrix} 1 & -0.1351 & 0.6407 \\ 0 & 0.7296 & 1.2814 \\ 0 & -0.3648 & 0.7296 \end{pmatrix} \tag{B.15}$$

which correspond to those of Eqs. (3) and (4) in the main text.

Through Eq. (A.2), one can observed that the following conversions are fulfilled:

$(0\bar{1}12)m \rightarrow (0003)n$

$(0003)m \rightarrow (0\bar{1}12)n$

$(0\bar{1}15)m \rightarrow (0\bar{1}15)n$ (B.16)

which correspond to what graphically evincible from Fig. B-1.

C. The relation between weak twins and conventional twins

The rearrangement of atomic positions during the propagation of specific interfaces can be used to explain different grain boundary structures and grain misorientations, as well as the formation of conventional twins [51,67]. In particular, a dual-step mechanism has been reported to govern the formation of TTW in Mg, where the nucleation of the predominant $\{10\bar{1}2\}$ twin is preceded by formation of $\{10\bar{1}1\}_m//(0001)_n$ weak interfaces that establish the lattice correspondence of the twin (90°) with a minor deviation from the ideal orientation (86.3°) [45,51–53]. Additionally, in Ref. [18], even if not specified by the authors, $\{10\bar{1}3\}$ twins and $\{10\bar{1}0\}_m \rightarrow \{10\bar{1}3\}_n$ weak interfaces are observed to form upon the growth of the $\{10\bar{1}1\}_m \rightarrow (0001)_n$ facets. From this, it appears that the prismatic→basal and the pyramidal I→basal plane transformations, belonging to the new class of deformation mechanism defined as *weak twinning* [22] (that encompasses the concept of *deformation graining*), are at the basis of the formation of conventional twin modes. Consequently, the pyramidal II→basal plane transformation may represent the initiating mechanism for the evolution of the $\{10\bar{1}5\}$ conventional twin.

Now, the concept and magnitude of s_g can be used to justify the formation of basal/prismatic interfaces before $\{10\bar{1}2\}$ twinning, and pyramidal I/ basal interfaces before $\{10\bar{1}1\}$ or $\{10\bar{1}3\}$ twinning. In particular, $s_g = 0.092$ for basal/prismatic, $s_g = 0.107$ for pyramidal I/basal, $s_g = 0.130$ for conventional $\{10\bar{1}2\}$ twin mode, and $s_g = 0.137$ for conventional $\{10\bar{1}1\}$ and $\{10\bar{1}3\}$ conventional twin modes. Interestingly, the basal/prismatic *weak twin*, (90°, *a*-axis), and the conventional $\{10\bar{1}2\}$ twinning mode, (86°, *a*-axis), have the same value of $\varepsilon_g = 0.130$ and same correspondence matrix [22, 45]. Analogously, also the pyramidal I/basal *weak twin*, (62°, *a*-axis), and the conventional $\{10\bar{1}1\}$ or $\{10\bar{1}3\}$ twinning modes, (56°, *a*-axis) and (64°, *a*-axis), respectively, have the same value of $\varepsilon_g = 0.137$ and same correspondence matrix. The correspondence matrix associated with the $(01\bar{1}1)_m \rightarrow (0002)_n$ plane transformation

$$\mathbf{C}_{hex}^{n\rightarrow m} = \begin{pmatrix} 1 & -1/4 & -3/4 \\ 0 & 1/2 & -3/2 \\ 0 & -1/2 & -1/2 \end{pmatrix}$$ (C.1)

converts also the $(01\bar{1}3)_m$ into $(01\bar{1}3)_n$ (conventional twin) and $(02\text{-}20)_m$ into $(01\bar{1}\text{-}3)_n$. Same considerations can be done for the pyramidal II/basal *weak twin* and the $\{10\bar{1}5\}$.

References

[1] M.H. Yoo, J.K. Lee, Deformation twinning in h.c.p. metals and alloys, Philos. Mag. A Phys. Condens. Matter, Struct. Defects Mech. Prop. 63 (1991) 987–1000, https://doi.org/10.1080/01418619108213931.

[2] J.W. Christian, S. Mahajan, Deformation twinning, Prog. Mater. Sci. 39 (1995) 1–157, https://doi.org/10.1016/0079-6425(94)00007-7.

[3] J. Koike, Enhanced deformation mechanisms by anisotropic plasticity in polycrystalline Mg alloys at room temperature, in: Metall. Mater. Trans. A Phys. Metall. Mater. Sci. (2005) 1689–1696, https://doi.org/10.1007/s11661-005-0032-4.

[4] N.M. della Ventura, P. Schweizer, A. Sharma, M. Jain, T.E.J. Edwards, J. J. Schwiedrzik, C. Peruzzi, R. Logé, J. Michler, X. Maeder, Micromechanical response of pure magnesium at different strain rate and temperature conditions: twin to slip and slip to twin transitions, Acta Mater. (2022), https://doi.org/10.1016/j.actamat.2022.118528.

[5] C.M. Byer, B. Li, B. Cao, K.T. Ramesh, Microcompression of single-crystal magnesium, Scr. Mater. 62 (2010) 536–539, https://doi.org/10.1016/j.scriptamat.2009.12.017.

[6] B. Syed, J. Geng, R.K. Mishra, K.S. Kumar, [0 0 0 1] Compression response at room temperature of single-crystal magnesium, Scr. Mater. 67 (2012) 700–703, https://doi.org/10.1016/j.scriptamat.2012.06.036.

[7] E. Lilleodden, Microcompression study of Mg (0 0 0 1) single crystal, Scr. Mater. 62 (2010) 532–535, https://doi.org/10.1016/j.scriptamat.2009.12.048.

[8] W.D. Russell, N.R. Bratton, Y.R. Paudel, R.D. Moser, Z.B. McClelland, C.D. Barrett, A.L. Oppedal, W.R. Whittington, H. Rhee, S. Mujahid, B. Paliwal, S.C. Vogel, H. El Kadiri, *In situ* characterization of the effect of twin-microstructure interactions on {1012} tension and {1011} contraction twin nucleation, growth and damage in magnesium, Metals 10 (2020) 1–23, https://doi.org/10.3390/met10111403 (Basel).

[9] M.R. Barnett, Twinning and the ductility of magnesium alloys. Part II. "Contraction" twins, Mater. Sci. Eng. A 464 (2007) 8–16, https://doi.org/10.1016/j.msea.2007.02.109.

[10] J. Peng, Z. Zhang, P. Guo, J. Huang, Y. Li, W. Zhou, Y. Wu, The effect of contraction twins and shear bands on the texture evolution during isothermal annealing and its effect on mechanical properties of AZ31 magnesium alloys, Mater. Sci. Eng. A 763 (2019), https://doi.org/10.1016/j.msea.2019.138100.

[11] P. Cizek, M.R. Barnett, Characteristics of the contraction twins formed close to the fracture surface in Mg-3Al-1Zn alloy deformed in tension, Scr. Mater. 59 (2008) 959–962, https://doi.org/10.1016/j.scriptamat.2008.06.041.

[12] Q. Yu, L. Qi, K. Chen, R.K. Mishra, J. Li, A.M. Minor, The nanostructured origin of deformation twinning, Nano Lett. 12 (2012) 887–892, https://doi.org/10.1021/nl203937t.

[13] M.A. Meyers, O. Vöhringer, V.A. Lubarda, The onset of twinning in metals: a constitutive description, Acta Mater. 49 (2001) 4025–4039, https://doi.org/10.1016/S1359-6454(01)00300-7.

[14] A. Chapuis, J.H. Driver, Temperature dependency of slip and twinning in plane strain compressed magnesium single crystals, Acta Mater. 59 (2011) 1986–1994, https://doi.org/10.1016/j.actamat.2010.11.064.

[15] Y. Liu, P. Mao, F. Zhang, Z. Liu, Z. Wang, Effect of temperature on the anisotropy of AZ31 magnesium alloy rolling sheet under high strain rate deformation, Philos. Mag. 98 (2018) 1068–1086, https://doi.org/10.1080/14786435.2018.1427896.

[16] H. Wang, P. Wu, S. Kurukuri, M.J. Worswick, Y. Peng, D. Tang, D. Li, Strain rate sensitivities of deformation mechanisms in magnesium alloys, Int. J. Plast. 107 (2018) 207–222, https://doi.org/10.1016/j.ijplas.2018.04.005.

[17] M.R. Barnett, A Taylor model based description of the proof stress of magnesium AZ31 during hot working, Metall. Mater. Trans. A Phys. Metall. Mater. Sci. A 34 (2003) 1799–1806, https://doi.org/10.1007/s11661-003-0146-5.

[18] B.Y. Liu, Z. Zhang, F. Liu, N. Yang, B. Li, P. Chen, Y. Wang, J.H. Peng, J. Li, E. Ma, Z.W. Shan, Rejuvenation of plasticity via deformation graining in magnesium, Nat. Commun. 13 (2022), https://doi.org/10.1038/s41467-022-28688-9.

[19] The theory of the crystallography of deformation twinning, Proc. R. Soc. London. Ser. A. Math. Phys. Sci. 288 (1965) 240–255, https://doi.org/10.1098/rspa.1965.0216.

[20] A. Ostapovets, A. Serra, Review of non-classical features of deformation twinning in HCP metals and their description by disconnection mechanisms, Metals 10 (2020) 1–20, https://doi.org/10.3390/met10091134 (Basel).

[21] C. Cayron, Hard-sphere displacive model of deformation twinning in hexagonal close-packed metals. Revisiting the case of the (56°,a) contraction twins in magnesium, Acta Crystallogr. Sect. A Found. Adv. 73 (2017) 346–356, https://doi.org/10.1107/S2053273317005459.

[22] C. Cayron, The concept of axial weak twins, Acta Mater. (2022), https://doi.org/10.2139/ssrn.4073482.

[23] C. Cayron, Hard-sphere displacive model of extension twinning in magnesium, Mater. Des. 119 (2017) 361–375, https://doi.org/10.1016/j.matdes.2017.01.047.

[24] G. Guillonneau, M. Mieszala, J. Wehrs, J. Schwiedrzik, S. Grop, D. Frey, L. Philippe, J.M. Breguet, J. Michler, J.M. Wheeler, Nanomechanical testing at high strain rates: New instrumentation for nanoindentation and microcompression, Mater. Des. 148 (2018) 39–48, https://doi.org/10.1016/j.matdes.2018.03.050.

[25] D. Casari, L. Pethö, P. Schürch, X. Maeder, L. Philippe, J. Michler, P. Zysset, J. Schwiedrzik, A self-aligning microtensile setup: Application to single-crystal GaAs microscale tension-compression asymmetry, J. Mater. Res. 34 (2019) 2517–2534, https://doi.org/10.1557/jmr.2019.183.

[26] S. Kalácska, J. Ast, P.D. Ispánovity, J. Michler, X. Maeder, 3D HR-EBSD Characterization of the plastic zone around crack tips in tungsten single crystals at the micron scale, Acta Mater. 200 (2020) 211–222, https://doi.org/10.1016/j.actamat.2020.09.009.

[27] E.W. Kelley, J.W.F. Hosford, Plane strain compression of magnesium and magnesium alloy crystals, Metall. Soc. Am. Inst. Min. Metall. Pet. Eng. Trans. 242 (1968) 5–13.

[28] H. Conrad, W.D. Robertson, Effect of temperature on the flow stress and strain-hardening coefficient of magnesium single crystals, JOM 9 (1957) 503–512, https://doi.org/10.1007/bf03397908.

[29] O. Bauer, O. Vollenbruck, G. Schikorr, E. Schmid, W. Boas, P. Beck, M. Polanyi, G. Wassermann, W. Fahrenhorst, G. Siebel, W. Stenzel, J. Weerts, K. Weißenbergr, E. Goens, G. Sachs, E. Schmid, Beiträge zur physik und metallographie des magnesiums, in: Mitteilungen Der Dtsch. Mater. (1932) 16–25, https://doi.org/10.1007/978-3-642-92044-8_2.

[30] R.E. Reed-Hill, W.D. Robertson, Deformation of magnesium single crystals by nonbasal slip, JOM 9 (1957) 496–502, https://doi.org/10.1007/bf03397907.

[31] A. Couret, D. Caillard, An *in situ* study of prismatic glide in HCP metals, Rev. Phys. Appl. 23 (1988) 667, https://doi.org/10.1051/rphysap:01988002304066700, 667.

[32] J. Jeong, M. Alfreider, R. Konetschnik, D. Kiener, S.H. Oh, *In-situ* TEM observation of {101̄2} twin-dominated deformation of Mg pillars: twinning mechanism, size effects and rate dependency, Acta Mater. 158 (2018) 407–421, https://doi.org/10.1016/j.actamat.2018.07.027.

[33] W.F. Hosford, E.W. Kelley, Plane-strain compression of magnesium and magnesium alloy crystals, Trans. Metall. Soc. AIME. 242 (1968) 5–13.

[34] H. Tonda, K. Nakamura, K. Takashima, {112̄2}<112̄3> slip in magnesium single crystal, J. Japan Inst. Light Met. 42 (1992) 765–771, https://doi.org/10.2464/jilm.42.765.

[35] A.G. Evans, R.D. Rawlings, The thermally activated deformation of crystalline materials, Phys. Status Solidi. 34 (1969) 9–31, https://doi.org/10.1002/pssb.19690340102.

[36] Z. Wu, W.A. Curtin, The origins of high hardening and low ductility in magnesium, Nature 526 (2015) 62–67, https://doi.org/10.1038/nature15364.

[37] K. Srivastava, J.A. El-Awady, Deformation of magnesium during c-axis compression at low temperatures, Acta Mater. 133 (2017) 282–292, https://doi.org/10.1016/j.actamat.2017.05.039.

[38] Y. Tang, J.A. El-Awady, Formation and slip of pyramidal dislocations in hexagonal close-packed magnesium single crystals, Acta Mater. 71 (2014) 319–332, https://doi.org/10.1016/j.actamat.2014.03.022.

[39] J. Ast, G. Mohanty, Y. Guo, J. Michler, X. Maeder, *In situ* micromechanical testing of tungsten micro-cantilevers using HR-EBSD for the assessment of deformation evolution, Mater. Des. 117 (2017) 265–266, https://doi.org/10.1016/j.matdes.2016.12.052.

[40] Y. Guo, J. Schwiedrzik, J. Michler, X. Maeder, On the nucleation and growth of {112̄2} twin in commercial purity titanium: *in situ* investigation of the local stress field and dislocation density distribution, Acta Mater. 120 (2016) 292–301, https://doi.org/10.1016/j.actamat.2016.08.073.

[41] J.R. Greer, J.T.M. De Hosson, Plasticity in small-sized metallic systems: Intrinsic versus extrinsic size effect, in: Prog. Mater. Sci. (2011) 654–724, https://doi.org/10.1016/j.pmatsci.2011.01.005.

[42] M.D. Uchic, D.M. Dimiduk, J.N. Florando, W.D. Nix, Sample dimensions influence strength and crystal plasticity, Science (80-.) 305 (2004) 986–989, https://doi.org/10.1126/science.1098993.

[43] M.D. Uchic, P.A. Shade, D.M. Dimiduk, Plasticity of micrometer-scale single crystals in compression, Annu. Rev. Mater. Res. 39 (2009) 361–386, https://doi.org/10.1146/annurev-matsci-082908-145422.

[44] N.M. Della Ventura, S. Kalácska, D. Casari, T.E.J. Edwards, A. Sharma, J. Michler, R. Logé, X. Maeder, {101̄2} twinning mechanism during *in situ* micro-tensile

[45] N.M. della Ventura, A. Sharma, S. Kalácska, M. Jain, T.E.J. Edwards, C. Cayron, R. Logé, J. Michler, X. Maeder, Evolution of deformation twinning mechanisms in magnesium from low to high strain rates, Mater. Des. 217 (2022), https://doi.org/10.1016/j.matdes.2022.110646.

loading of pure Mg: Role of basal slip and twin-twin interactions, Mater. Des. 197 (2021), https://doi.org/10.1016/j.matdes.2020.109206.

[46] M.D. Nave, M.R. Barnett, Microstructures and textures of pure magnesium deformed in plane-strain compression, Scr. Mater. 51 (2004) 881–885, https://doi.org/10.1016/j.scriptamat.2004.07.002.

[47] M. Bevis, A.G. Crocker, Twinning modes in lattices, 313 (1969) 590–529. doi:10.1098/rspa.1969.0208. Royal Society.

[48] M.R. Barnett, Z. Keshavarz, A.G. Beer, X. Ma, Non-Schmid behaviour during secondary twinning in a polycrystalline magnesium alloy, Acta Mater. 56 (2008) 5–15, https://doi.org/10.1016/j.actamat.2007.08.034.

[49] H. Yoshinaga, T. Obara, S. Morozumi, Twinning deformation in magnesium compressed along the C-axis, Mater. Sci. Eng. 12 (1973) 255–264, https://doi.org/10.1016/0025-5416(73)90036-0.

[50] L. Jiang, J.J. Jonas, A.A. Luo, A.K. Sachdev, S. Godet, Twinning-induced softening in polycrystalline AM30 Mg alloy at moderate temperatures, Scr. Mater. 54 (2006) 771–775, https://doi.org/10.1016/j.scriptamat.2005.11.029.

[51] L. Jiang, M. Gong, J. Wang, Z. Pan, X. Wang, D. Zhang, Y.M. Wang, A. Ciston, A.M. Minor, M. Xu, X. Pan, T.J. Rupert, S. Mahajan, E.J. Lavernia, I.J. Beyerlein, J.M. Schoenung, Visualization and validation of twin nucleation and early-stage growth in magnesium, Nat. Commun. (2022) 13, https://doi.org/10.1038/s41467-021-27591-z.

[52] B.Y. Liu, J. Wang, B. Li, L. Lu, X.Y. Zhang, Z.W. Shan, J. Li, C.L. Jia, J. Sun, E. Ma, Twinning-like lattice reorientation without a crystallographic twinning plane, Nat. Commun. 5 (2014), https://doi.org/10.1038/ncomms4297.

[53] K.Y. Xie, K. Hazeli, N. Dixit, L. Ma, K.T. Ramesh, K.J. Hemker, Twin boundary migration mechanisms in quasi-statically compressed and plate-impacted mg single crystals, Sci. Adv. 7 (2021), https://doi.org/10.1126/sciadv.abg3443.

[54] C. Cayron, Complements to mügge and friedel's theory of twinning, Metals 10 (2020), https://doi.org/10.3390/met10020231 (Basel).

[55] M. Bevis, A.G. Crocker, Twinning shears in lattices, Proc. R. Soc. Lond. Ser. A Math. Phys. Sci. 304 (1968) 123–134, https://doi.org/10.1098/rspa.1968.0077.

[56] Y. Guo, H. Abdolvand, T.B. Britton, A.J. Wilkinson, Growth of {112̄2} twins in titanium: A combined experimental and modelling investigation of the local state of deformation, Acta Mater. 126 (2017) 221–235, https://doi.org/10.1016/j.actamat.2016.12.066.

[57] B. Leu, M. Arul Kumar, P.F. Rottmann, K.J. Hemker, I.J. Beyerlein, Micromechanical fields associated with irregular deformation twins in magnesium, J. Mater. Eng. Perform. (2022), https://doi.org/10.1007/s11665-022-07196-3.

[58] H. Abdolvand, A.J. Wilkinson, Assessment of residual stress fields at deformation twin tips and the surrounding environments, Acta Mater. 105 (2016) 219–231, https://doi.org/10.1016/j.actamat.2015.11.036.

[59] T.A. Parthasarathy, S.I. Rao, D.M. Dimiduk, M.D. Uchic, D.R. Trinkle, Contribution to size effect of yield strength from the stochastics of dislocation source lengths in finite samples, Scr. Mater. 56 (2007) 313–316, https://doi.org/10.1016/j.scriptamat.2006.09.016.

[60] S.H. Oh, M. Legros, D. Kiener, G. Dehm, *In situ* observation of dislocation nucleation and escape in a submicrometre aluminium single crystal, Nat. Mater. 8 (2009) 95–100, https://doi.org/10.1038/nmat2370.

[61] D. Hull, D.J. Bacon. Introduction to dislocations, 2011, https://doi.org/10.1016/C2009-0-64358-0. Butterworth-Heinemann.

[62] S. Ando, M. Tsushida, H. Kitahara, Deformation behavior of magnesium single crystal in c-axis compression and a-axis tension, in: Mater. Sci. Forum (2010) 699–702, https://doi.org/10.4028/www.scientific.net/MSF.654-656.699.

[63] L. Wen, P. Chen, Z.F. Tong, B.Y. Tang, L.M. Peng, W.J. Ding, A systematic investigation of stacking faults in magnesium via first-principles calculation, Eur. Phys. J. B 72 (2009) 397–403, https://doi.org/10.1140/epjb/e2009-00365-2.

[64] G.D. Sim, G. Kim, S. Lavenstein, M.H. Hamza, H. Fan, J.A. El-Awady, Anomalous hardening in magnesium driven by a size-dependent transition in deformation modes, Acta Mater. 144 (2018) 11–20, https://doi.org/10.1016/j.actamat.2017.10.033.

[65] Z. Zhang, Twinning and its related work hardening during the ambient extrusion of a magnesium alloy, Mater. Sci. Eng. A 577 (2013) 125–137, https://doi.org/10.1016/j.msea.2013.03.078.

[66] C. Cayron, Groupoid of orientational variants, Acta Crystallogr. Sect. A Found. Crystallogr. 62 (2006) 21–40, https://doi.org/10.1107/S010876730503686X.

[67] Y. He, B. Li, C. Wang, S.X. Mao, Direct observation of dual-step twinning nucleation in hexagonal close-packed crystals, Nat. Commun. 11 (2020), https://doi.org/10.1038/s41467-020-16351-0.